2022-06

Applying group theory to the study of a carbon trimer defect in hexagonal boron nitride

Aligholamioskooee, Omid

UNIVERSITY OF CALGARY

Applying group theory to the study of a carbon trimer defect in hexagonal boron nitride

by

Omid Aligholamioskooee

A THESIS
SUBMITTED TO THE FACULTY OF GRADUATE STUDIES
IN PARTIAL FULFILMENT OF THE REQUIREMENTS FOR THE
DEGREE OF MASTER OF SCIENCE

GRADUATE PROGRAM IN PHYSICS AND ASTRONOMY

CALGARY, ALBERTA
JUNE, 2022

Abstract

Hexagonal boron nitride (h-BN) is a promising platform for quantum information processing due to its potential to host optically active defects with attractive optical and spin properties [1]. Recent studies suggest that carbon trimers might be the defect responsible for single-photon emission in the visible spectral range in h-BN. In this theoretical study, we combine group theory together with density-functional theory (DFT) calculations to predict the properties of the neutral C_2C_N carbon trimer defect. We find the multi-electron states of this defect along with possible radiative and nonradiative transitions assisted by the spin-orbit and the spin-spin interactions. We also investigate the Hamiltonian for external magnetic-field and ground-state hyperfine interactions. Lastly, we use the results of our investigation in a Lindblad (or Gorini–Kossakowski–Sudarshan–Lindblad) master-equation model to predict an optically detected magnetic resonance signal and the $g^2(\tau)$ correlation function. Our findings can have important outcomes in quantum information applications such as quantum repeaters used in quantum networks and quantum sensing.

[1] In this thesis I have used materials from our latest paper [1] in several chapters, with the permission of all authors and the journal.

Acknowledgements

Throughout my master's, I have received assistance from many people.

First and foremost, I would like to thank my supervisor, Professor Christoph Simon. Since the admission process and during my master's program, Christoph has been nothing but supportive, patient, and responsive, making working with him highly productive and delightful. Christoph gave me the freedom to choose and develop my project but was always available to share his insightful advice when needed. He provided a calm and tension-less environment where I could focus only on science and my project and not worry about any distractions.

Second, I would like to thank my friends. Starting a life in a new country and during a pandemic had many challenges, but they helped me overcome the obstacles. I met Hadi when I began my master's degree, and since then, he has been a great friend and helped me like a big brother. He has helped my academic and personal growth, and I am incredibly grateful for that. Additionally, my other dear friend Omid and his company in hiking and other physical activities have allowed me to manage the stress of life and maintain my mental and physical health. I would also like to thank my other friends and colleagues, Sara, Faezeh, Parisa, Ali, Ken, Farid, and Stephen.

Third, I appreciate the efforts of the supervisory and examining committee members, including Professor Dennis Salahub, Professor Barry Sanders, and Professor Nasser Moazzen-Ahmadi. Dennis is also a co-author of our paper, where his and Professor Claudia Gomes da Rocha's expertise and advice were vital for our project.

Finally, I cannot express enough gratitude to my parents for their love and support. They gave me the freedom to pursue my curiosity and introduced me to exciting aspects of science. This accomplishment would not have been possible without them. Thank you!

List of published papers

Omid Golami, Kenneth Sharman, Roohollah Ghobadi, Stephen C. Wein, Hadi Zadeh-Haghighi, Claudia Gomes da Rocha, Dennis R. Salahub, and Christoph Simon. *Ab initio* and group theoretical study of properties of a carbon trimer defect in hexagonal boron nitride. Phys. Rev. B, 105:184101, May 2022.

(Golami is the preferred family name that I am using in my papers)

Table of Contents

List of Figures

List of Tables

List of Symbols, Abbreviations, and Nomenclature

Symbol	Definition
h-BN	Hexagonal boron nitride
ODMR	Optically detected magnetic resonance
DFT	density functional theory
MO	Molecular orbital
QD	Quantum dot
QKD	Quantum key distribution
TMDC	Transition metal dichalcogenide
NV	nitrogen vacancy
C_2C_N	$C_NC_BC_N$ carbon trimer
C_2C_B	$C_BC_NC_B$ carbon trimer
ZPL	Zero-phonon line
IR	irreducible representation
CNOT	Controlled NOT
2D	2 dimensional
UV	Ultraviolet
PBE	Perdew-Burke-Ernzerhof
HSE	Heyd-Scuseria-Ernzerhof

Chapter 1

Introduction

A quantum system, as opposed to a classical system, has some unique characteristics, including superposition states, where a binary system can be in a superposition of state zero and state one at the same time, and entanglement, where a group of particles are prepared in a way that the state of each of these particles, even when separated by a large distance, cannot be described independently [5]. These properties give an advantage to a quantum system for solving certain problems. For example, Shor's algorithm potentially allows a quantum computer to find the prime factors of an integer almost exponentially faster than a classical computer [6].

These advantages have motivated researchers to explore different systems for implementing a quantum information processing unit. There are some properties that these quantum systems should possess [7]. First, decoherence causes a superposition state to collapse due to the interaction with its environment. Hence, it is important to isolate the quantum system from its environment and increase the coherence time so that a required process can be performed before decoherence happens. Second, any quantum system should be scalable, correctable, and controllable in order to be useful for applications [8]. Scalability will allow a quantum system to increase in size and number of qubits, or quantum bits, where the advantage of a quantum algorithm is apparent. Additionally, a quantum system should be correctable because background noise can cause errors in calculations, and these errors should be detected and corrected. Lastly, we should be able to initialize, manipulate, and readout a qubit so that we can perform quantum gates and do quantum calculations.

Some of the most promising and developed systems for quantum information processing and communication, based on the mentioned criteria, are atom-like spins in solids[9], superconducting circuits [10], ion traps [11], and topological systems [12]. While they are still being developed, each of them has its own advantages

and disadvantages. Superconducting qubits are one of the leading platforms for quantum computation, where they use the robustness of superconductivity and the nonlinearity of Josephson junctions [13]. Their performance has been improved by several orders of magnitude during the past two decades, making them promising for building large-scale error-corrected quantum computers [14]. In a trapped ion system, charged particles are confined in free space by electromagnetic waves [15]. Qubits stored in the electronic states of ions have suitable coherence times, can be prepared and measured with close to 100% efficiency (overall success probability), and are entangled with each other through the Coulomb interaction or remote photonic interconnects [11]. Finally, while all other methods try to isolate a qubit from its environment to avoid decoherence, topological systems use a different approach. They use nonabelian phases of matter to store and manipulate quantum information in a nonlocal manner, which protects them from errors and decoherence from the interaction with the environment [12]. Several experiments have shown the existence of Majorana Fermions [16], which are proposed to be used for topological quantum computation [17]. But there is still more work needed to develop techniques to make, control, and manipulate these topological qubits.

We will discuss atom-like spins in more detail in the next sections. My research has been focused on photonics quantum technology, with an emphasis on atom-like spins in solid-state materials and their role as spin-photon interfaces for applications in quantum networks and communication. Quantum photonics, where a quantum of light, or a photon, is used for quantum information processing, is one of the leading platforms in quantum computation and is a natural choice for quantum communication and metrology because of its unique properties, including the ability to transfer the quantum state at the speed of light and through optical fibers with high coherence [18]. Consequently, we will focus on the role of photonics in the applications of quantum technology, atom-like spins in solids, and spin-photon interfaces.

1.1 Applications of quantum information

The applications of quantum information can be categorized into the three main fields of computation, communication, and sensing [19]. We will look at them individually and discuss their photonic implementations.

1.1.1 Quantum computation

A quantum processing unit will allow us to use the power of quantum mechanics for tasks such as factorizing a number to its prime numbers by using Shor's algorithm, searching databases by using Grover's algorithm [20], and simulating quantum systems to solve many-body physics problems [21]. In order to use photons in quantum information applications, the quantum state should be encoded in degrees of freedom of a photon, which includes polarization and temporal or spatial modes. As we will see, indistinguishable single

photons play a crucial role in some of the leading quantum systems for quantum computation with promising scalability [22].

In the quantum circuit model, a quantum gate is an operator that acts on one or more qubits. Quantum gates are usually classified based on the number of qubits they operate on, such as one-qubit, two-qubit, and so on. In practice, it is easier to produce a small set of gates and use them to construct any given unitary operator. Any set of gates that has this property is called a universal set of gates; for example, the set of Toffoli and Hadamard gates is a universal set of gates, where the Toffoli gate is a three-qubit controlled-controlled-NOT gate, and the Hadamard gate is a one-qubit gate that maps the basis states $|0\rangle$ to $\frac{|0\rangle+|1\rangle}{\sqrt{2}}$ and $|1\rangle$ to $\frac{|0\rangle-|1\rangle}{\sqrt{2}}$ [23]. Alternatively, a two-qubit CNOT (controlled-NOT) gate combined with one-qubit gates construct another set of universal gates [21], which makes CNOT gates important for many quantum information processing applications. A CNOT gate flips the state of the second qubit if the first qubit, or the control qubit, is in state one, and it does nothing if the control qubit is in state zero. It has been shown that a CNOT gate can be implemented using auxiliary single-photon sources and detectors without the need for nonlinear optical elements [24]. Hence, they allow scalable quantum computation and show the importance of single-photon emitters. However, there are different schemes for making a CNOT gate without using single photons. But they have their challenges because of the need for a highly nonlinear material [18].

Although the circuit-model-based quantum computation had great progress, it requires a significant number of gates and high entanglement generation rates, which makes it hard to implement. Alternatively, a measurement-based or a one-way quantum computer is mathematically equivalent to the circuit-based model [25] but offers more promising advantages for implementing it physically [26]. A one-way quantum computer uses an entangled state of multiple qubits, called a cluster-state, where single-photon sources are vital for some optical schemes [27]. Thus, it shows the importance of single-photon sources for these alternative methods.

1.1.2 Quantum communication

Transmitting quantum information between various nodes would provide unprecedented secure communications. The laws of quantum mechanics guarantee that an arbitrary unknown quantum state cannot be copied, which is proven by the no-cloning theorem [28]. Additionally, the measurement of an unknown quantum state, if it is not compatible with the measurement, will perturb the system. Therefore, by using quantum systems, one can increase the security of communication and, in the case of an eavesdrop, potentially detect it [29]. An essential part of secure communication is sharing secure keys between the nodes. In this regard,

quantum key distribution (QKD) methods enable two nodes to share a secure key and use it to achieve a highly-secure information transition [30].

One of the problems of a quantum communication channel where the signal consists of more than one photon is that an eavesdropper can perform a photon number splitting attack by storing the additional photons and later obtain full information about the shared key between the nodes [31]. Although there are different ways to solve this problem, one of the solutions to prevent this attack is using single-photon sources [32]. Hence, single-photon emitters are vital for some QKD applications, such as certain device-independent QKD protocols [33].

1.1.3 Quantum sensing

Quantum sensing allows physical measurements with high precision, which means that the measurements will have closer and less dispersed results compared to each other. Fundamentally, Heisenberg's uncertainty principle puts a limit on the precision of a measurement, but classical devices are far from this fundamental precision. It has been shown that by using quantum characteristics such as squeezed and entangled states, and single-photon sources, it is possible to beat the precision of classical measurements [34, 35]. Again, in quantum sensing applications, single-photon sources are necessary [36]. Some quantum sensing systems use interference to achieve high resolution [37], while others use properties of atom-like spins in solids to measure the magnetic field, electric field, or temperature with high spatial resolution [38].

1.2 Quantum networks

In general, a network, based on Ref. [39], is defined as: "A network is a group of interacting parties, where each of the members potentially wants to interact with any of the other members." And a telecommunication network consists of nodes that are connected through telecommunication links. Additionally, a quantum network is a telecommunication network where the links allow transferring of quantum information. A large-scale quantum network or the quantum internet [40], will not only be used for quantum communication applications but also can be useful for distributed quantum computation [41], and quantum sensing [42, 43]. The nodes in these quantum networks can be photon emitters and detectors used, for example, for quantum key distribution, or can be quantum computers, where distributed quantum computing will be possible [39]. However, other types of nodes, such as quantum repeaters, are also needed for large-scale networks. In a quantum network, photon loss during transmission limits the size of the network. Although the no-cloning theorem is an advantage for security, it prevents us from using amplifiers to strengthen a signal and send it over longer distances. However, there are other solutions, such as quantum repeaters, where quantum

entanglement is used to extend a quantum channel over longer distances [44]. In this approach, one splits the distance between the two nodes into several nodes with smaller separations. Each of these nodes contains quantum devices; for example, in some suggested schemes, they need a photon pair generator and a quantum memory to store information [45]. In this scheme, each adjacent node produces a pair of photons, stores one of them, and sends the other to a central beamsplitter. Detection of a single photon means the stored states are entangled. Here, the use of single-photon sources significantly increases the entanglement distribution rate [46].

1.2.1 Spin-photon interface

Each node in a quantum network mediated by entangled photons should fulfill three main requirements. First, it needs an efficient interface between qubits and photons, where, for example, a high fraction of photons are emitted into the zero-phonon line, in order to generate entangled photons at high rates. Second, they need quantum memory to store information while generating and distributing entanglement. Third, they need several quantum memories with the capability to perform high-fidelity gates between them, which is needed for error correction and other multi-qubit operations [47].

There are several promising systems used as nodes of quantum networks, such as atomic-based qubits, including atomic ensembles, single atomic ions [48], and single neutral atoms [49], and less studied superconducting-based systems [50]. Further, atom-like color centers, such as defects in diamond, are among the leading systems that fulfill all of these requirements, whereas compared to atoms or ions, they do not require trapping. Their spin-photon interface, electronic structure, and spin selective optical transitions allow remote entanglement between their spin state and a photonic state. This makes solid-state color centers even more interesting for various applications. Additionally, that is why there are many theoretical and experimental attempts to understand the structure and spin-photon interface of new centers, hopefully with better properties, in emerging materials by using group theory and density-functional theory (DFT) for the theory part and electron paramagnetic resonance and optically detected magnetic resonance (ODMR) experiments for the experiment part [51].

1.2.2 Atom-like spins in solids

As we discussed, single-photon emitters have a significant role in different quantum applications, and atom-like spins, or artificial atoms, are among the most promising single-photon sources [52]. Furthermore, other optical and spin characteristics of these artificial atoms, such as their spin-photon interface, give them advantages in certain applications. Many atom-like spins with promising optical and spin properties have

been found and studied in different platforms, including semiconductor quantum dots (QDs) and atomic color centers. Self-assembled semiconductor QDs have shown promising performance in photon generation rates, optical coherence, range of spectral tunability, and integration into nanostructures [53]. Additionally, high spin-photon and spin-spin entanglement generation rates, quantum teleportation, quantum-state transfer, quantum relays, and on-chip integration with polarization-demultiplexing waveguides have been realized experimentally using indium arsenide QDs. Although some electron or hole spins in QDs have coherence times of a few milliseconds, some solid-state color centers have much higher spin coherence times. Furthermore, some solid-state color centers couple to nearby nuclear spins with high coherence times [54], making a quantum register, where this cluster of ancillary qubits is hard to form in QD systems. Quantum registers are required for many applications, such as quantum error correction or as a quantum memory for quantum communication. Consequently, researchers have been interested in understanding and improving these color centers.

Color centers are optically active defects or impurities in a solid-state lattice. One of the most promising and studied color centers is the nitrogen-vacancy (NV) center in diamond. This defect is constructed by substituting a carbon in the diamond lattice with a nitrogen atom and removing another nearby carbon, which results in a vacancy. The NV center in its negatively charged form has a multilevel electronic structure with a triplet ground state, which has been used for initialization, control, and readout. Additionally, the interaction of the electron spin with the nuclear spin of the nearby ^{13}C impurities in the lattice or the nitrogen atom allows the NV center to be a quantum register with impressive properties. In this respect, coherence time exceeding 1 second at room temperature has been realized for individually addressable nuclear spins [55]. Recent advances with NV centers include the realization of a three-node entanglement-based quantum network [56], the realization of a two-node quantum network over a distance of 1.3 km [57], the realization of a single electron spin coupled to a multi-qubit nuclear-spin [58], and quantum error correction on a continuously encoded qubit by real-time feedback [59].

These achievements with NV center have triggered the exploration of other defects in solid-state systems [60] in order to increase the fidelity and efficiency of the quantum gates and, eventually, the scalability of the system, which includes other defects in diamond, such as silicon-vacancy [61] and germanium vacancy [62], or defects in other solid-state materials such as silicon carbide [63], and van der Waals materials [64]. Each of these defects and systems has some advantages over others. In particular, insulator or semiconductor van der Waals materials with a large enough bandgap have gained more attention in recent years because of their novel properties. Among them, the most promising 2-dimensional (2D) materials are hexagonal boron nitride (h-BN) and transition metal dichalcogenides (TMDCs). Monolayer TMDC materials are atomically thin MX_2 type semiconductors, where a layer of transition metal atoms (M), such as molybdenum and tungsten,

is placed between two layers of chalcogen atoms (X), such as sulfur, selenium, and tellurium. Some of these monolayer TMDC materials, such as tungsten diselenide (WSe_2) and molybdenum diselenide ($MoSe_2$), have a direct bandgap. Optically active defects in TMDCs have been reported by different experimentalists [65, 66, 67], while more research is needed to understand the true nature of these defects.

1.3 Defects in h-BN

Similarly, ultrabright and polarized single-photon emission from color centers in two-dimensional (2D) hexagonal boron nitride (h-BN) has been recently observed at room temperature [68]. Hexagonal boron nitride has attracted attention for several reasons. First, it has a relatively large bandgap of around 6 eV [69, 70, 71] which allows it to host many defects [72, 73, 74, 75, 76]. Second, because of its 2D nature, it is promising for heterogeneous assembly and on-chip integration into devices [77, 4]. Third, some defects in h-BN might have high sensitivity to the environment because of their location at the surface, which is advantageous for quantum sensing applications [78]. Finally, defects in h-BN are the only known solid-state sources that can display Fourier transform limited lines at room temperature [79]. If the Fourier transform of an emitter's temporal profile matches its spectral lineshape, then the emitter resonance does not fluctuate during the timescale of emission. This implies that quantum coherence is maintained so that the emitter can be used for many quantum protocols.

Although there have been various measurements of single-photon emitters in h-BN, the true atomic structure of most of these emitters remains unknown [80, 81]. Therefore, we have done theoretical calculations to understand the electronic structure of one of the most promising defects in h-BN. Similar to previously studied defects in solids, such as the NV center [3, 82, 83] and the silicon-vacancy center [84, 85] in diamond, or the boron vacancy in h-BN [81], we have used a combination of group theory and DFT calculations, which are strong tools to theoretically investigate new defects and help with identifying defects. DFT is one of the most used *ab initio*, or first principles, approaches for studying properties of defects in solids, such as electronic structure, energy levels, formation energy, different couplings, and radiative or nonradiative transition rates [86]. Additionally, group theory uses the symmetries of the defect to simplify the matrix elements and provides a good intuition of the electronic structure. Group theory is discussed in more detail in Chapter 2.

It has been shown that visible range single-photon emitters in h-BN originate from carbon-related defects [80]. Jara *et al.* [87] suggest that the neutral C_2C_N and C_2C_B carbon trimer defects might have zero-phonon line (ZPL) energies of 1.62 and 1.65 eV, respectively, and a phonon sideband of around 160 meV, which is typically found in many experiments [80, 88]. However, a new study suggests that the C_2C_B defect might

have a ZPL energy of 1.36 eV [89]. This energy is too far from the visible range, and so we focus only on the C_2C_N defect where both studies agree on a ZPL energy of around 1.6 eV. However, more studies are needed to understand the C_2C_B defect.

In this study, we explore the electronic structure of the C_2C_N defect in 2D h-BN and find the possible radiative and nonradiative transitions to model the observed lines. To do so, we combine group theory analysis with DFT calculations [90, 91]. We determine the symmetry-adapted molecular orbitals (MOs) using group theory analysis. Then, we use DFT results to determine the relative energy ordering of these orbitals [3]. Next, we obtain the total orbital and spin multi-electron states by filling the lowest energy MOs, which gives us the ground state. Exciting electrons to the higher energy MOs gives us the excited states [82]. We calculate the total energy of the electronic structures with DFT, and the difference between these energies gives us the transition energies between defect states.

We then consider the spin-orbit, the spin-spin, and external magnetic-field interactions and find matrix elements of the Hamiltonian, where group theory decreases the complexity by reducing the number of nonzero elements. Furthermore, we look at the interaction between the defect and the electromagnetic field and find nonvanishing matrix elements to derive the optical transitions. Combining this with the spin-orbit and the spin-spin Hamiltonians gives us possible nonradiative transitions assisted by the spin-orbit and the spin-spin interactions [81]. We also examine the hyperfine interaction of the ground state with a possible nearby nuclear spin [83]. Finally, we look at the dynamics of this system and simulate the ODMR signal predicted by the Lindblad (or Gorini–Kossakowski–Sudarshan–Lindblad) master equation [92].

Chapter 2

Group theory

2.1 Introduction

As we discussed, the electronic structure of many of the defects in solids is unknown. However, there are some tools that help us understand their electronic structure, such as group theory. Group theory is a powerful tool used to simplify and give intuition about the energy levels and calculate the matrix elements of different perturbations, such as spin-orbit or spin-spin couplings. In this section, we will see that the Coulombic Hamiltonian is in the diagonal form in the symmetry-adapted basis. Additionally, we will be able to find the zero matrix elements of various interactions only using group theory calculation, which hugely decreases the number of calculations [1].

2.2 Definitions

First, let us briefly discuss the definitions of a group and a class of a group [93].

Definition 2.1. A group is a set of elements, $\mathcal{G} = \{g_1, g_2, g_3, ...\}$, together with a binary operator, called group multiplication and denoted by " $\cdot$ " here, that associates a combination of two elements to an element, denoted by $g_1 \cdot g_2$. This multiplication must satisfy closure and associativity, and the group must include the identity and inverse elements.

Definition 2.2. A class of a group, $\mathcal{G}$, that contains element g_1 is a set that contains all conjugates of g_1, where g_1 is conjugate to g_3 if there exists an element g_2 in $\mathcal{G}$ such that $g_1 = g_2 \cdot g_3 \cdot g_2^{-1}$, i. e. $Cl(g_1) = \{g_2 \cdot g_1 \cdot g_2^{-1} : g_2 \in \mathcal{G}\}$.

[1] The approach of this chapter is based on the "Group Theory and Quantum Mechanics" book [93].

2.3 Theory of group representations

A d-dimensional representation is a homomorphic map of a group $\mathcal{G}$ onto a group of nonsingular $d \times d$ matrices $\Gamma(g)$, with matrix multiplication as the group multiplication operator. That is, a d-dimensional representation is a map $\rho : \mathcal{G} \to \Gamma(g)$, such that for all g_1 and g_2 in $\mathcal{G}$, one has $\Gamma(g_1 \cdot g_2) = \Gamma(g_1)\Gamma(g_2)$ [94].

2.3.1 Reducible and irreducible representations

A representation is called reducible if it is possible to reduce the matrices representing all the elements of the group to block form with the same block structure by the same similarity transformation. Otherwise, the representation is called irreducible. Also, it can be shown that the number of classes is equal to the number of irreducible representations.

Now we can introduce one of the important theorems that is a basis for the group theoretical calculation performed in this thesis.

Theorem 2.3. ***The great orthogonality theorem [93, p. 23]***

"If we consider all the inequivalent, irreducible, unitary representations of a group, then

$$\sum_R \Gamma^{(i)}(R)^*_{\mu\nu}\Gamma^{(j)}(R)_{\alpha\beta} = \frac{h}{l_i}\delta_{ij}\delta_{\mu\alpha}\delta_{\nu\beta}, \tag{2.1}$$

where in the summation R runs over all group elements E, A_2, ..., A_h and l_i is the dimensionality of $\Gamma^{(i)}$."

We can think of each element of the irreducible representation i, $\Gamma^{(i)}(g)_{\mu\nu}$, as a vector in the vector space of the group elements. Then, the great orthogonality theorem says that these vectors will be orthogonal to each other.

2.3.2 The Character of a representation

If $\Gamma^{(j)}$ is a d-dimensional representation of a group $\mathcal{G}$, then the character of a group element, g_1, in this representation is defined as

$$\chi^{(j)}(g_1) = Tr(\Gamma^{(j)}(g_1)) = \sum_{i=1}^{l_j} \Gamma^{(j)}(g_1)_{ii}, \tag{2.2}$$

where l_j is the dimension of $\Gamma^{(j)}$. The character of all of the elements of a class of a group is equal since the class elements are conjugates of each other.

In the Eq. (2.1), if we set $\mu = \nu$ and $\alpha = \beta$, and sum over μ and α, we will end up with the following

equation for characters:

$$\sum_{g\in\mathcal{G}} \chi^{(i)}(g)^* \chi^{(j)}(g) = h\delta_{ij}. \tag{2.3}$$

2.4 Transformation operators

Since we are interested in symmetry groups, we need to first study the orthogonal transformation operators on coordinates. These transformations can be written as

$$x_i' = \sum_j R_{ij} x_j, \tag{2.4}$$

where $\mathbf{R}$ is a real orthogonal matrix. In quantum mechanical systems, we deal with wave functions; therefore, it will be helpful to introduce a new isomorphic group, where the elements, $P_{\mathbf{R}}$, operate on functions instead of coordinates. This transformation is defined as

$$P_{\mathbf{R}} f(\mathbf{R}\vec{x}) = f(\vec{x}), \tag{2.5}$$

where we have used Wigner's convention which means $P_{\mathbf{R}}$ compensates the changes made by $\mathbf{R}$. One can prove that $P_{\mathbf{R}}$ is isomorphic to $\mathbf{R}$ by showing that $P_{\mathbf{RS}} = P_{\mathbf{R}} P_{\mathbf{S}}$. Since $\mathbf{R}$ and $P_{\mathbf{R}}$ are isomorphic, they will have the same irreducible representations.

Let us consider a physical system with Hamiltonian H, where it is invariant under operator $P_{\mathbf{R}}$. This means that the Hamiltonian and the operator commute. Now let us assume that $\phi_i^{(n)}$ is an eigenfunction of H with eigenvalue E_n in a degenerate subspace of size l_i; thus it can easily be shown that applying $P_{\mathbf{R}}$ on this eigenfunction results in a function that is also an eigenfunction of H with the same eigenvalue: $H(P_{\mathbf{R}}\phi_i^{(n)}) = P_{\mathbf{R}}(H\phi_i^{(n)}) = E_n(P_{\mathbf{R}}\phi_i^{(n)})$. Therefore, we can write $P_{\mathbf{R}}\phi_i^{(n)}$ as a combination of all of the eigenfunctions in the degenerate subspace, and by applying all the symmetry operators that commute with H on a given eigenfunction, we can generate all of the eigenfunctions in the same degenerate subspace. Consequently, we can represent the effect of these operators by matrices given by

$$P_{\mathbf{R}}\phi_j^{(r)} = \sum_{i=1}^{l_r} \phi_i^{(r)} \Gamma_{ij}^{(r)}(\mathbf{R}), \tag{2.6}$$

where we can say ϕ_i^r transforms as the ith row of the representation r. It can be shown that these matrices form irreducible representations of the symmetry group of the Hamiltonian [93].

Now that we know these functions form a basis for the Hilbert space, we will study methods that help us produce symmetry-adapted orbitals, which will be used later. We can multiply both sides of the equation

above by $\Gamma^{(r')}_{i'j'}(\mathbf{R})^*$, sum over $\mathbf{R}$, and use the great orthogonality theorem to get

$$\sum_{\mathbf{R}} \Gamma^{(r')}_{i'j'}(\mathbf{R})^* P_{\mathbf{R}} \phi^{(r)}_j = \frac{h}{l_r} \phi^{(r)}_{i'} \delta_{jj'} \delta_{rr'}. \tag{2.7}$$

Now, we can define the operator

$$\mathscr{P}^{(r)}_{ij} = \frac{l_r}{h} \sum_{\mathbf{R}} \Gamma^{(r)}_{ij}(\mathbf{R})^* P_{\mathbf{R}}. \tag{2.8}$$

One can see that applying $\mathscr{P}^{(r)}_{ij}$ on $\phi^{(r)}_j(\mathbf{R})$, gives $\phi^{(r)}_i(\mathbf{R})$, but applying it on any other basis functions of the irreducible representations, will result in zero.

The projection operator

In Eq. (2.8), if we impose $i = j$ and then sum over i, we will have the projection operator that projects functions into the representation r. This operator is given by

$$P^{(r)} = \frac{l_r}{h} \sum_{\mathbf{R}} \chi^{(r)}(\mathbf{R})^* P_{\mathbf{R}}. \tag{2.9}$$

We will use this equation in Chapter 5 to find symmetry-adapted molecular orbitals.

2.5 Symmetry groups

So far, we have mostly discussed groups at the abstract level; however, one of the powerful uses of group theory is when we look at the symmetry groups [95].

Definition 2.4. A symmetry group is a group including all the transformations that an object is invariant under them, where the group multiplication is defined as function composition.

As we have discussed, we are interested in defects in solid-state lattices because of their promising properties for quantum applications. Thus, we need to know the operators of the symmetry group in a Bravais lattice. A Bravais lattice is an infinite array of points which are invariant under translation operators described in 3-dimension by $\vec{T} = n_1\vec{a}_1 + n_2\vec{a}_2 + n_3\vec{a}_3$, where n_i are integers and $\vec{a}_i$ are the primitive vectors. These translations are not necessarily the only operators covering the lattice. For example, there might be rotational or reflective operators in the symmetry group.

Definition 2.5. A symmetry sub-group of a Bravais lattice that includes only elements that can be carried out by fixing a point in the lattice is called a point group.

The elements of the point group and the translation operators together construct the space group, which includes all the transformation operators of the lattice. There are three fundamental operators constructing the point groups, including rotations around an axis through the origin, reflections with respect to planes containing the origin, and inversions with respect to the origin.

There is a standard notation, called the Schoenflies notation [96], to specify the symmetry elements and point groups in three dimensions. There are many symmetry point groups, but we will only focus on the C_{nv} group, which is relevant to our research. Other point groups can be found in textbooks. The C_{nv} symmetry group has only one n-fold rotation axis with the addition of n vertical reflections (reflections with respect to planes that include the principal symmetry axis). Therefore, its symmetry elements are the identity operator (E), rotations through $2\pi/n$ (C_n), and n reflections in a vertical plane (σ_v).

2.6 Matrix elements and applications of group theory

In physical systems, group theory is a powerful tool for finding the matrix elements of the Hamiltonian of the system. Here, we will discuss a theorem and its generalization that are used to find the vanishing matrix elements [93]. They are essential for simplifying and calculating the matrix elements of the Hamiltonian, particularly when the Hilbert space is big and it is time-consuming to calculate each matrix element.

Theorem 2.6. ***[93, p. 80]***

"Matrix elements of an operator H which is invariant under all operations of a group vanish between functions belonging to different irreducible representations or to different rows of the same unitary representation."

If H was the Hamiltonian of a physical system, this theorem implies that the Hamiltonian is diagonals in the basis functions that transform according to the ith row of the irreducible representation, $\phi_i^{(r)}$. This is a powerful tool for studying the energy levels of a physical system. One can use the projection operator, Eq. (2.9), to find the projection of the electron wave functions into the functions that transform according to a specific irreducible representation of the symmetry group, called the symmetry-adapted molecular orbitals, where the Hamiltonian is diagonalized.

Additionally, by using this theorem, we can have a selection rule to eliminate many of the matrix elements based on symmetry-related calculations. It is used when the operator H is not symmetric under all operators of the symmetry group. For example, if there is a perturbation in the system and it reduces the symmetry of the system. So, let us assume an operator, H', transforms according to the irreducible representation $\Gamma_{H'}$. It can be shown that its matrix element $\langle \psi_i^{(r')} | H' | \phi_j^{(r)} \rangle$ is zero unless $\Gamma_{H'} \times \Gamma^{(r)}$ includes $\Gamma^{(r')}$. Equivalently, the matrix element is zero unless $\Gamma^{(1)}$ is found in $\Gamma^{(r')} \times \Gamma^{(H')} \times \Gamma^{(r)}$. This is a powerful tool that allows

us to reduce the number of calculations by considering the symmetries of a defect and finding the vanishing matrix elements of the Hamiltonian. Its proof can be found in group theory books.

As we have shown, group theory is a powerful tool to study point defects in solids, and we will use the theorems from this chapter in Chapter 5 for the theoretical calculations.

Chapter 3

Open quantum systems

If a quantum system is interacting with the environment, the evolution of this system will not necessarily be unitary [1]. Therefore, we need to study the time evolution of the system in a general manner. A general evolution is given by a map from the initial density matrix to a density matrix at an arbitrary time. In this chapter, we will study the general form of these maps, where they preserve the properties of a density matrix. Next, we will derive the Lindblad (or Gorini–Kossakowski–Sudarshan–Lindblad) master equation. The Lindblad master equation is a differential equation of the density matrix, which allows us to numerically calculate the time evolution of the density matrix in an open quantum system [92]. Understanding this technique will be helpful later when predicting optical signals for a quantum system we studied.

3.1 Kraus operator

Now, let us find what should be the general form of a map that preserves the properties of the density matrix. This map is called a quantum channel and is defined below [35].

Definition 3.1. A quantum channel is a map from density operators to density operators.

This means that quantum channels should satisfy the following axiomatic properties:

1. Linearity
2. Hermiticity preservation
3. Complete positivity
4. Trace preservation

[1] The approach of this chapter is taken from the "Quantum Computation" lecture notes of John Preskill [97].

The following theorem, Kraus' theorem, shows the general form of quantum channels [21]. We will use this theorem for the remainder of this chapter.

Theorem 3.2. ***The Kraus representation theorem [98, p. 65]***

"Any operator $\rho \to \mathcal{E}(\rho)$ in a space of dimensions N^2 that obeys the properties of Linearity, Trace preservation, Hermiticity preservation, and complete positivity, can be written in the form:

$$\mathcal{E}(\rho) = \sum_{k=1}^{K} M_k \rho M_k^\dagger, \qquad \textit{with} \qquad \sum_{k=1}^{K} M_k^\dagger M_k = \mathbb{I} \tag{3.1}$$

where $K \leq N_s^2$ is the Kraus number (with N_s the dimension of the system)."

The quantum channel, $\mathcal{E}$, is an operator that acts on operators, ρ. Hence, it is called a superoperator. Also, it is good to note that there can be different sets of Kraus operators as long as they obey the completeness relation. These sets of Kraus operators are related to each other with a unitary transformation.

3.2 Markovian evolution

When the evolution of the states is not unitary, there is no guarantee that calculating the infinitesimal evolution of the density matrix and then integrating it over time will give us the correct evolution of the density matrix over larger timescales. Because the system might have a memory; then, the state of the system can depend on the state of the system from much earlier times. However, if the evolution of the system is Markovian, which means that $\rho(t + dt)$ only depends on $\rho(t)$ and dt, then we can calculate a differential equation of the density matrix and find $\rho(t)$ at any given time.

Fortunately, in many cases, the Markovian approximation is valid for the systems [99]. This is when the time that it takes for the environment to forget about the system is much shorter than the time scales of the evolution that we are interested in. Therefore, we can have a quantum channel, as shown below, which determines the density matrix at time $t + dt$ based on the density matrix at time t.

$$\rho(t + dt) = \mathcal{E}(\rho(t); dt) \tag{3.2}$$

3.3 Lindblad master equation

Now, we will derive the Lindblad master equation by assuming the Markovian approximation [100, 101]. We start with writing the density matrix up to the first order of dt, where we have

$$\rho(t+dt) = \rho^{(0)}(t) + dt\,\rho^{(1)}(t) + O(dt^2). \tag{3.3}$$

By using the Kraus' theorem, Eq. (3.1), we can write

$$\rho(t+dt) = \sum_k M_k(dt)\rho(t)M_k^\dagger(dt). \tag{3.4}$$

The Eqs. (3.3) and (3.4) imply that the Kraus operators should be in the form of

$$M_k = M_k^{(0)} + \sqrt{dt}M_k^{(1)} + dt\,M_k^{(2)} + O(dt^{3/2}). \tag{3.5}$$

Since the Kraus operators are not unique, we can chose

$$M_0 = \mathbb{I} + dt\,L_0 + O(dt^2), \tag{3.6}$$

and

$$M_k = \sqrt{dt}L_k + O(dt) \tag{3.7}$$

for $k > 0$ without loss of generality. As shown below, it is possible to write any arbitrary operator as a sum of a Hermitian and anti-Hermitian operator.

$$T = \frac{(T+T^\dagger) + (T-T^\dagger)}{2} = H + A, \tag{3.8}$$

where $H = \frac{(T+T^\dagger)}{2}$ is a Hermitian operator and $A = \frac{(T-T^\dagger)}{2}$ is an anti-Hermitian operator. Thus, we can write $L_0 = K - iH$, where both K and H are Hermitian operators. By plugging these into Eq. (3.4), we have

$$\begin{aligned}
\rho(t+dt) &= M_0(dt)\rho(t)M_0^\dagger(dt) + \sum_{k>0} M_k(dt)\rho(t)M_k(dt) \\
&= (\mathbb{I} + dt(-iH+K))\,\rho(t)\,(\mathbb{I} + dt(iH+K)) + dt\sum_{k>0}\left(L_k\rho(t)L_k^\dagger\right) + O(dt^2) \\
&= \rho(t) - i\,dt[H,\rho(t)] + dt(K\rho(t) + \rho(t)K) + dt\sum_{k>0}\left(L_k\rho(t)L_k^\dagger\right) + O(dt^2).
\end{aligned} \tag{3.9}$$

Additionally, we can use the completeness relation,

$$\sum_k M_k^\dagger M_k = \mathbb{I} + dt\left(2K + \sum_{k>0} L_k^\dagger L_k\right) = \mathbb{I}, \tag{3.10}$$

which gives K in terms of $\{L_k\}$:

$$K = -\frac{1}{2}\sum_{k>0} L_k^\dagger L_k. \tag{3.11}$$

By replacing K from Eq. (3.11) into Eq. (3.9), rearranging the first term on the right hand side, and dividing by dt, we will get

$$\dot{\rho} = \mathcal{L}(\rho) = -i[H,\rho] + \sum_{k>0}\left(L_k\rho L_k^\dagger - \frac{1}{2}\{L_k^\dagger L_k, \rho\}\right), \tag{3.12}$$

which is called the Lindblad (or Gorini–Kossakowski–Sudarshan–Lindblad) master equation. As it is clear from this equation, the choice of L_0 was necessary for separating the unitary evolution of the density matrix, $-i[H,\rho]$, from the rest of it. The second term in the right hand side of the Lindblad master equation describes the interaction of the system with the environment. The operators L_k are called jump operators. As an example, if there is an optically allowed transition in a two level system, we will need two jump operators to describe the evolution of the system, one for absorbing a photon and exciting the system and one for emitting a photon and decaying to the ground state.

Finally, we can solve this equation and find the density matrix at any arbitrary time [92], which is given by

$$\rho(t) = e^{\mathcal{L}t}\rho(0). \tag{3.13}$$

All of the assumptions and conditions have not been covered in the derivation above [102]. In quantum optics, the weak coupling limit derivation is mainly used, which includes three approximations called Born, Markov, and rotating wave [103]. The Born approximation assumes that the system and environment interact weakly [104], while the rotating-wave approximation allows neglecting fast-oscillating terms [92]. The Markov approximation has already been discussed.

We will use the master equation (Eq. (3.12)) and Eq. (3.13) in Section 5.11 in order to simulate the optically detected magnetic resonance of the carbon trimer defect and will discuss more computational details in the same chapter. The optically detected magnetic resonance is explained in the next chapter, which will be useful for understanding our simulation in Section 5.11.

Chapter 4

Optically detected magnetic resonance

Optically detected magnetic resonance (ODMR) is a double resonance spectroscopy technique which is a special case of electron paramagnetic resonance technique [105]. Since the first ODMR experiment by Schmidt and van der Waals in 1968, [106], it has been developed and used on many systems. In recent years, ODMR has been used for studying the properties of the electron spin in defects in solid-state materials, such as the negatively charged nitrogen-vacancy (NV^-) center in diamond [107]. In this chapter, we will first discuss the ODMR technique used on the well-studied NV^- center to get familiar with this technique. Then, we will briefly discuss an ODMR experiment performed on a defect in h-BN. In the next chapter, we will discuss the methods and results of simulating the ODMR signal for the specific defect in the h-BN that we have studied. It will be an important experimental test for our theoretical and computational calculations of that defect.

4.1 Nitrogen vacancy center

The NV^- color center in diamond is a well-known defect in a solid-state system with many applications in quantum computation, communication, and sensing [108, 109]. This defect is a substitution of a nitrogen atom instead of a carbon atom in a diamond lattice with an additional adjacent vacancy. Its electronic structure is shown in Fig. 4.1(a) and includes a triplet ground state ($^3A_2$), an excited triplet state (^3E), and two singlet states (^1E and $^1A_1$) between the triplet states [82]. The transition between the ground and excited triplet states is optically allowed. Thus, one can use resonant lasers to pump the electrons from the ground state to the excited triplet state while conserving their spin. These excited electrons can decay through the same optical transition by emitting a photon or through the intersystem crossing to the singlet states, which is nonradiative. The decay from spin ± 1 sublevels of the excited triplet state to the singlet

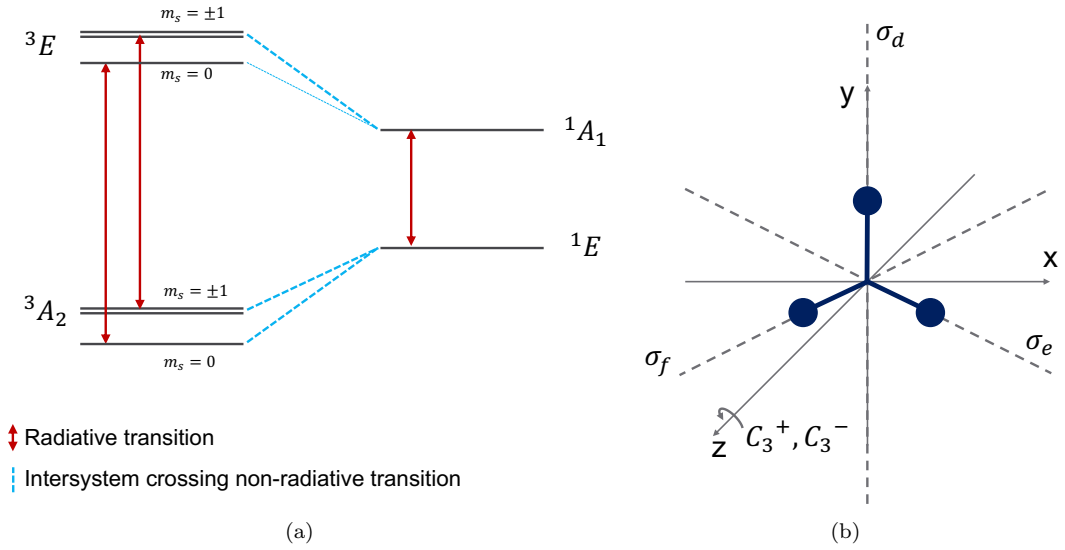

Figure 4.1: (a) Electronic structure of the NV^- color center in diamond. The $^3A_2$ and ^3E states are triplet states while ^1E and $^1A_1$ are singlet states. The intersystem crossing from the spin 0 sublevel of the excited triplet state to the singlet state is weaker compared to the intersystem crossing from the spin ± 1 sublevels. (b) Symmetry operators of the C_{3v} symmetry group, including two three-fold rotations and three reflections, which is the symmetry point group of the NV^- color center.

state is stronger than the decay from the spin 0 sublevel. Therefore, most of the electrons in the spin 0 sublevel will decay optically, whereas electrons in the spin ± 1 sublevels can decay nonradiatively with a 40% probability. Therefore, a resonant laser will eventually populate the spin-zero sublevel [110].

Now, if there is an additional microwave maser in resonance with the ground state spin sublevels, it will drive the transition between these sublevels and reduce the intensity of the fluorescence signal. This will result in a dip in the measured photoluminescence spectrum. It is used in sensing applications since this signal is affected by the external magnetic field and temperature.

In the case of the NV^- color center, we can use the ODMR signal in applications because we know the energy levels and structure of this defect. However, in our case, we will use this technique to predict results that are based on the electronic structure of the defect that we have studied. This will test our theoretical and computational calculations.

4.2 Room-temperature ODMR experiment with h-BN

There are several experiments measuring the ODMR signal from defects in h-BN, whereas the origin of many of them is still unknown [111, 112].

Here, we will discuss the work of Stern et al. [4], which will help us understand the experimental setup of an ODMR spectroscopy experiment. In the model they proposed for the defect that the signal

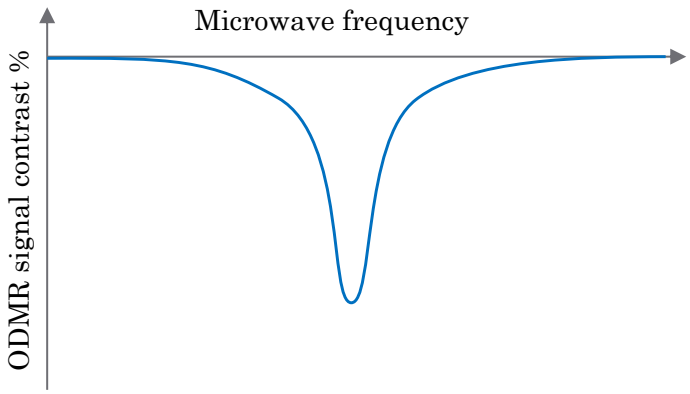

Figure 4.2: An example of an ODMR signal with a dip. There will a dip or peak corresponding to any possible resonance in the energy levels.

originated from, there are two triplet states, similar to the NV^- center, and one singlet state responsible for the nonradiative intersystem crossing. The zero-field splitting of the triplet states was too small to detect in their experiment; therefore, they have used an additional external magnetic field to split the sublevels further. As a consequence, the contrast in the fluorescence signal as a function of the microwave frequency (Fig. 4.2), which is the ODMR signal, will have a dip (or peak in some cases) when the microwave frequency is in resonance with the splitting caused by the magnetic field.

The ODMR signal depends on the electronic structure and energy levels of the defect. Therefore, if it is detectable, it is a good test for identifying a defect and comparing the theoretical model with the experiment and is important for understanding the spin-photon interface of the defect. In the next chapter, we will come back to the ODMR signal, where we simulate the ODMR signal for the carbon trimer defects that we have studied.

Chapter 5

Ab initio and group theoretical study of properties of a carbon trimer defect in hexagonal boron nitride

5.1 Introduction

The contents of this chapter and the appendices are copied from our latest paper and have been modified slightly [1]. My contribution to this work are the group theory calculations, matrix element calculations and the ODMR simulation parts, while all the DFT calculations have been performed by the second author, Kenneth Sharman.

In this chapter we demonstrate our approach and calculations used for understanding the C_2C_N defect in hexagonal boron nitride (h-BN). This chapter is organized as follows: In Sec. 5.2 we discuss the symmetry of the C_2C_N defect and determine the symmetry-adapted molecular orbitals (MOs). Then we investigate multi-electron states (Sec. 5.3), the spin-orbit interaction (Sec. 5.4), the spin-spin interaction (Sec. 5.5), spin-orbit and spin-spin mediated transitions (Sec. 5.6), selection rules for the transitions (Sec. 5.7), external magnetic-field effect (Sec. 5.8), and hyperfine interaction (Sec. 5.9). In Sec. 5.10 we found radiative and some nonradiative transition rates, then in Sec. 5.11 we simulate the optically detected magnetic resonance (ODMR) spectra and the $g^2(\tau)$ second-order correlation function. Finally, we discuss computational methods in Sec. 5.12. Matrix elements of all of the interactions and more configurations for the ODMR simulations are given in the appendix.

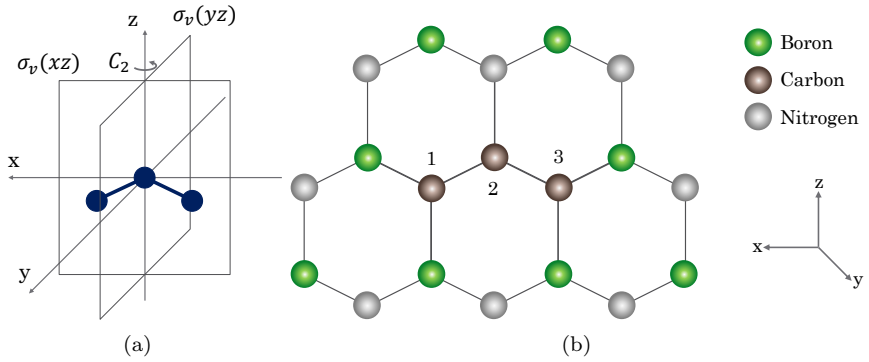

Figure 5.1: (a) Symmetry operators of C_{2v} point group, apart from the identity operator (E), shown for a carbon trimer defect. The first one is $C_2(z)$ which is a rotation by π around the z axis. The other two are reflections through xz and yz planes, respectively, $\sigma_v(xz)$ and $\sigma_v(yz)$. Note that the three carbon atoms are in the xz plane. (b) The atomic configuration of the C_2C_N defect in 2D h-BN sheet.

5.2 Molecular orbitals

The atomic configuration of the C_2C_N defect is shown in Fig. 5.1(b), where C_2 denotes the C_BC_N carbon dimer, and C_N denotes a substitution of a nitrogen atom with a carbon atom. In order to find the symmetry group of the defect, it is important to know if the defect is in- or out-of-plane, as some defects might be distorted out of the plane [113]. A recent study suggests that distortion from the plane for the C_2C_N defect is negligible and that it has a planar structure [89]. Thus, this defect has C_{2v} symmetry, which is supported by defect wave functions as in Fig. 5.2(a).

The ground-state configuration of carbon is $1s^2 2s^2 2p^2$. The planarity of the defect implies that carbon atoms will have sp^2 hybridization. In sp^2 hybridization, the $2s$ orbital is mixed with only two of the three available $2p$ orbitals. The third $2p$ orbital remains unhybridized and out of the plane and in the $\hat{y}$ direction, which is also confirmed by our DFT calculations shown in Fig. 5.2(a).

Each carbon atom of the C_2C_N defect shares three of its valence electrons with nearby atoms in the lattice; therefore, they each have one unpaired electron. Thus, the dangling bonds of the defect are π bonds, and they are denoted $\{\pi_1, \pi_2, \pi_3\}$.

C_{2v}	E	$C_2(z)$	$\sigma_v(xz)$	$\sigma_v(yz)$	Linear	Quadratic	Cubic
A_1	1	1	1	1	z	x^2, y^2, z^2	z^3, x^2z, y^2z
B_2	1	-1	-1	1	y, R_x	yz	yz^2, y^3, x^2y
B_1	1	-1	1	-1	x, R_y	xz	xz^2, x^3, xy^2
A_2	1	1	-1	-1	R_z	xy	xyz

Table 5.1: Character table for C_{2v} point group. E, $C_2(z)$, $\sigma_v(xz)$, $\sigma_v(yz)$ are symmetry operators. A_1, B_2, B_1, and A_2 are irreducible representations of the point group.

Now, we need to find the symmetry-adapted MOs of this defect, which can be found by either group theory or DFT (DFT results are shown in Fig. 5.2(a)). Comparing both results provides us with their symmetry and energy ordering, which are essential for our calculations. The MOs are eigenfunctions of the Coulombic Hamiltonian. Therefore, we apply the projection operator,

$$\phi_r = P^{(r)}\sigma_i = \frac{l_r}{h}\sum_e \chi_e^{(r)} R_e \pi_i, \tag{5.1}$$

with a specific irreducible representation (IR) on our dangling bonds to find symmetrized MOs [93]. Here, $P^{(r)}$ is the projection to the representation r, l_r is the dimension of the representation r, h is the number of symmetry group members, $\chi_e^{(r)}$ is the character of the operator e in the representation r, R_e is the symmetry operator, and π_i is the dangling bond i. According to the character table of C_{2v} point group (Table 5.1), b and b' MOs transform according to IR B_2. They are defined as

$$b = \alpha\pi_2 + \frac{\beta}{\sqrt{2}}(\pi_1 + \pi_3), \tag{5.2}$$

$$b' = \beta^*\pi_2 - \frac{\alpha^*}{\sqrt{2}}(\pi_1 + \pi_3), \tag{5.3}$$

where α and β are overlap integrals and $|\alpha|^2 + |\beta|^2 = 1$. There is another MO that transforms as IR A_2, defined as

$$a = \frac{1}{\sqrt{2}}\{\pi_1 - \pi_3\}. \tag{5.4}$$

5.3 Multi-electron states

We use DFT to find the energy of each of the MOs discussed above and their energy ordering. The defect wave functions in Fig. 5.2(a) obtained from the DFT calculations show that the MO with the lowest energy transforms as IR B_2, so it represents the b MO. This is because, according to the symmetry operators in Fig. 5.1(a), this MO is antisymmetric under $C_2(z)$ and $\sigma_v(xz)$, and symmetric under E and $\sigma_v(yz)$. The next MO with higher energy transforms as IR A_2, because it is antisymmetric under $\sigma_v(xz)$ and $\sigma_v(yz)$, and symmetric under E and $C_2(z)$. Therefore, it represents the a MO. Finally, the one with the highest energy transforms as IR B_2 similar to the first one, and thus it represents the b' MO. Based on a previous study, the MOs in the ground state and the first excited state lie inside the bandgap [87]. Our *ab initio* calculations show that the MOs in the next two excited states are also in the bandgap.

Multi-electron states are composed by filling the MOs with three unpaired electrons of the defect, starting

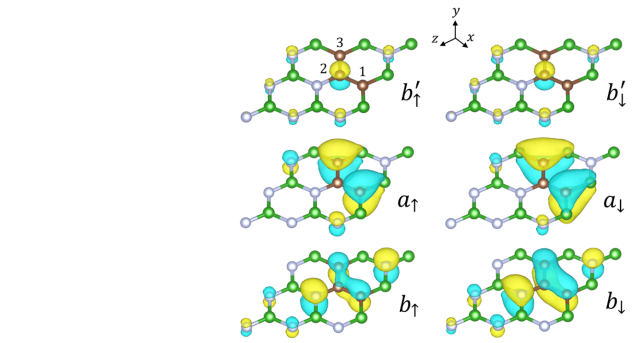

(a)

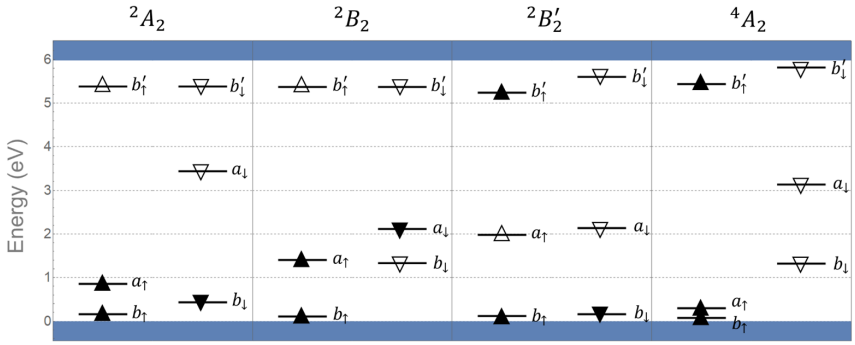

(b)

Figure 5.2: (a) Ground-state wave functions of the C_2C_N defect. The positive (negative) components of each wave function are visualized by the yellow (blue) lobes. The corresponding symmetries are best represented when the b and a orbitals are plotted here at an isosurface level of $\pm 0.007\,\text{Å}^{-3}$, and the b' orbital at $\pm 0.0002\,\text{Å}^{-3}$. The orbital energies increase from the bottom to the top, i. e., $E_b < E_a < E_{b'}$. Only the atoms and contributions to the wave function which are close to the C_2C_N defect are shown for simplicity. The carbon atoms are brown, boron atoms are green, and nitrogen atoms are grey. The diagrams were produced using VESTA [2]. (b) Defect levels of the ground state and single-configuration excited states in the fundamental bandgap of h-BN. The occupied (unoccupied) levels are denoted by solid (empty) triangles.

from the lowest energy b MO. The b MO will be fully occupied with two electrons in the ground state, and the a MO will be half occupied. This configuration will form a spin doublet because the half occupied a MO can be either spin up or down. So its spin multiplicity will be equal to two. This lowest multi-electron state has the configuration $[b]^2[a]^1[b']^0$ which transforms as IR A_2. Other excited multi-electron states are produced by exciting each of these electrons to higher MOs. The $[b]^1[a]^2[b']^0$ and $[b]^2[a]^0[b']^1$ configurations are also spin doublets, similar to the ground state, and transform according to IR B_2. But the other excited state $[b]^1[a]^1[b']^1$ needs careful consideration. Since it is the addition of three spin-1/2 orbitals, it will have three irreducible spin representations, including one quartet state and two doublet states with multiplicities four, two, and two, respectively. These states all transform as IR A_2. The corresponding electronic configurations of these states are given in Table 5.2 and the energy levels of the first four single-configuration states are given in Fig. 5.2(b).

Configuration	$^{2S+1}\Gamma$	Clebsch-Gordan states	Label
$[b]^2[a]^1[b']^0$	$^2A_2$	$\lvert b\bar{b}a\rangle, \lvert b\bar{b}\bar{a}\rangle$	$\mathcal{A}^{0,d}_{\pm 1/2}$
$[b]^1[a]^2[b']^0$	$^2B_2$	$\lvert ba\bar{a}\rangle, \lvert \bar{b}a\bar{a}\rangle$	$\mathcal{B}^{1,d}_{\pm 1/2}$
$[b]^2[a]^0[b']^1$	$^2B_2'$	$\lvert b\bar{b}b'\rangle, \lvert b\bar{b}\bar{b}'\rangle$	$\mathcal{B}^{2,d}_{\pm 1/2}$
$[b]^1[a]^1[b']^1$	$^4A_2$	$\lvert bab'\rangle, \lvert \bar{b}\bar{a}\bar{b}'\rangle$	$\mathcal{A}^{3,q}_{\pm 3/2}$
		$\frac{1}{\sqrt{3}}(\lvert \bar{b}ab'\rangle + \lvert b\bar{a}b'\rangle + \lvert ba\bar{b}'\rangle)$	$\mathcal{A}^{3,q}_{+1/2}$
		$\frac{1}{\sqrt{3}}(\lvert b\bar{a}\bar{b}'\rangle + \lvert \bar{b}a\bar{b}'\rangle + \lvert \bar{b}\bar{a}b'\rangle)$	$\mathcal{A}^{3,q}_{-1/2}$
	$^2A_2'$	$\frac{1}{\sqrt{6}}(\lvert \bar{b}ab'\rangle + \lvert b\bar{a}b'\rangle - 2\lvert ba\bar{b}'\rangle)$	$\mathcal{A}^{3,d'}_{+1/2}$
		$\frac{1}{\sqrt{6}}(\lvert \bar{b}a\bar{b}'\rangle + \lvert \bar{b}\bar{a}b'\rangle - 2\lvert b\bar{a}\bar{b}'\rangle)$	$\mathcal{A}^{3,d'}_{-1/2}$
	$^2A_2''$	$\frac{1}{\sqrt{2}}(\lvert b\bar{a}b'\rangle - \lvert \bar{b}ab'\rangle)$	$\mathcal{A}^{3,d''}_{+1/2}$
		$\frac{1}{\sqrt{2}}(\lvert b\bar{a}\bar{b}'\rangle - \lvert \bar{b}a\bar{b}'\rangle)$	$\mathcal{A}^{3,d''}_{-1/2}$

Table 5.2: Configuration of total wave functions. Some of these states are entangled states which need careful consideration when calculating their energy using DFT. Spin-down electrons in an orbital are shown with a line over them. In the label column, calligraphic letters $\mathcal{A}$ and $\mathcal{B}$ represent IRs A_2 and B_2, respectively. Also, d and q in the superscript stand for doublet and quartet states, respectively. Prime and double prime in IRs of each state is used just to distinguish them from other states with the same IR.

5.4 Spin-orbit interaction

The spin-orbit interaction is the sum of the Larmor and Thomas interaction energy which is given by

$$\begin{aligned} H_{\mathrm{SO}} &= \sum_k \frac{\hbar}{2m_{\mathrm{e}}^2 c^2}(\boldsymbol{\nabla}_k V \times \boldsymbol{p}_k)\cdot\left(\frac{\boldsymbol{s}_k}{\hbar}\right) \\ &= \sum_k \boldsymbol{l}_k \cdot \left(\frac{\boldsymbol{s}_k}{\hbar}\right), \end{aligned} \tag{5.5}$$

where V is the electric potential energy of the nucleus, $\hbar$ is the reduced Planck constant, m_e is the electron rest mass, c is the speed of light in vacuum, $\boldsymbol{s}_k$ is the spin of electron k, $\boldsymbol{p}_k$ is the momentum of electron k, and k sums over all electrons [82]. By utilizing group theory, we omit the vanishing components of the matrix elements of l_k. The elements $\langle\phi_i|l_k|\phi_j\rangle$ are nonvanishing only if $\Gamma(\phi_i)\otimes\Gamma(l_k)\otimes\Gamma(\phi_j)\supset\Gamma^{A_1}$, where Γ is the irreducible representation. Since $\boldsymbol{l}$ is proportional to $\boldsymbol{r}\times\boldsymbol{p}$, it transforms as (B_2, B_1, A_2). Based on Table 5.3, only l_y, which transforms as IR B_1, will have nonzero values. Therefore,

$$H_{\mathrm{SO}} = \sum_k l_k^{(y)} \left(\frac{s_k^{(y)}}{\hbar}\right). \tag{5.6}$$

Because of the symmetry of the system and according to Table 5.3, we know that only elements in the form of $\langle B_2|H_{\mathrm{so}}|A_2\rangle$ and their complex conjugate will be nonzero. Also, since we know $s_y = \frac{1}{2i}(s_+ - s_-)$, only the states whose spin are different by one will yield nonzero values. After considering these symmetry constraints, we obtain the matrix elements provided in the appendix (Sec. A).

O^{A_1}	B_2	A_2
B_2	×	0
A_2	0	×

O^{B_2}	B_2	A_2
B_2	0	0
A_2	0	0

O^{B_1}	B_2	A_2
B_2	0	×
A_2	×	0

O^{A_2}	B_2	A_2
B_2	0	0
A_2	0	0

Table 5.3: Matrix elements of operators with specific symmetries in the $\{B_2, A_2\}$ manifold where × indicates a nonzero value.

5.5 Spin-spin interaction

The spin-spin interaction is described by

$$\begin{aligned} H_{\mathrm{ss}} &= \frac{\mu_0\gamma_{\mathrm{e}}^2\hbar^2}{4\pi}\sum_{i>j}\frac{1}{r_{ij}^3}[\boldsymbol{s}_i\cdot\boldsymbol{s}_j - 3(\boldsymbol{s}_i\cdot\hat{\boldsymbol{r}}_{ij})(\boldsymbol{s}_j\cdot\hat{\boldsymbol{r}}_{ij})] \\ &= \frac{\mu_0\gamma_{\mathrm{e}}^2\hbar^2}{4\pi}\sum_{i>j}[\boldsymbol{s}_i\cdot\hat{D}_{ij}\cdot\boldsymbol{s}_j] \\ &= \frac{\mu_0\gamma_{\mathrm{e}}^2\hbar^2}{4\pi}\sum_{i>j}[\hat{\boldsymbol{s}}_{ij}^{(2)}\otimes\hat{D}_{ij}^{(2)}]^{(0)}, \end{aligned} \tag{5.7}$$

where $r_{ij} = r_i - r_j$ is the distance between electrons i and j, $\hat{\boldsymbol{r}}_{ij}$ is the unit vector from electron i to electron j, $\boldsymbol{s}_i$ is the spin of nucleus i, μ_0 is the vacuum permeability, and γ_{e} is the electron gyromagnetic ratio [114].

$\hat{\boldsymbol{s}}_{ij}^{(2)} = \hat{\boldsymbol{s}}_i^{(1)} \otimes \hat{\boldsymbol{s}}_j^{(1)}$ is a rank two spin tensor and $\hat{D}_{ij}$ is a traceless second-rank tensor operator defined as,

$$\hat{D}_{ij} = \frac{1}{r_{ij}^5} \begin{pmatrix} r_{ij}^2 - 3x_{ij}^2 & -3x_{ij}y_{ij} & -3x_{ij}z_{ij} \\ -3x_{ij}y_{ij} & r_{ij}^2 - 3y_{ij}^2 & -3y_{ij}z_{ij} \\ -3x_{ij}z_{ij} & -3y_{ij}z_{ij} & r_{ij}^2 - 3z_{ij}^2 \end{pmatrix}. \tag{5.8}$$

Writing the interaction in this form simplifies the calculations of matrix elements.

For spherically symmetric states, traceless $\hat{D}_{ij}$ means all three diagonal elements vanish. However, due to the lack of spherical symmetry of this defect, we should consider these elements in this magnetic dipole-dipole interaction. More details and matrix elements of the spin-spin Hamiltonian are provided in the appendix Sec. A.2.

5.6 Spin-orbit and spin-spin induced transitions

For the spin-orbit interaction, as we discussed before, only the matrix elements in the form of $\langle B_2|H_{\text{so}}|A_2\rangle$ and their complex conjugate will be nonzero. This indicates that there are no matrix elements in degenerate manifolds of $\{\mathcal{A}^{0,d}, \mathcal{B}^{1,d}, \mathcal{B}^{2,d}, \mathcal{A}^{3,q}\}$. Therefore, there is no mixing due to the spin-orbit coupling. However, we have possible spin-orbit induced transitions between the states in these manifolds, which are $\mathcal{B}^{1,d} \leftrightarrow \mathcal{A}^{0,d}, \mathcal{B}^{2,d} \leftrightarrow \mathcal{A}^{0,d}, \mathcal{B}^{1,d} \leftrightarrow \mathcal{A}^{3,q}$, and $\mathcal{B}^{2,d} \leftrightarrow \mathcal{A}^{3,q}$. A transition is called nonradiative, when the energy difference is gained or dissipated as thermal energy, for example, as lattice vibrations or phonons in solid-state materials [115]. Therefore, as discussed in Refs. [116, 117], these nonradiative transitions can happen in two steps. First, spin-orbit assisted transition occurs for example from $\mathcal{B}^{2,d}$ to a vibrational excited state of $\mathcal{A}^{3,q}$. This is followed by a relaxation to the vibrational ground-state, for example, via the emission of one or more phonons caused by the interaction between phonons. Such a process will be possible if there is an overlap between the initial vibrational level of $\mathcal{B}^{2,d}$ and the excited vibrational level of $\mathcal{A}^{3,q}$. A transition between two energy levels, however, is said to be radiative when it is carried out by absorbing or emitting a photon, which we will discuss in the next section.

Similarly and based on the findings of the previous section, the spin-spin interaction has no matrix element in the degenerate manifold of $\{\mathcal{A}^{0,d}, \mathcal{B}^{1,d}, \mathcal{B}^{2,d}\}$. However, there are nonzero matrix elements of the spin-spin interaction in the quartet state manifold. $\mathcal{D}_0$ is the diagonal, and $\mathcal{E}_3$ is the off-diagonal term. Hence, spin-spin interaction breaks the degenerate quartet states into two states and separates them by $2\mathcal{D}_0$. Also, the nondiagonal terms in the same manifold mix these two states. There are also possible spin-spin induced transitions between the states in these manifolds, which are $\mathcal{A}^{0,d} \leftrightarrow \mathcal{A}^{3,q}, \mathcal{B}^{1,d} \leftrightarrow \mathcal{A}^{3,q}, \mathcal{B}^{2,d} \leftrightarrow \mathcal{A}^{3,q}$.

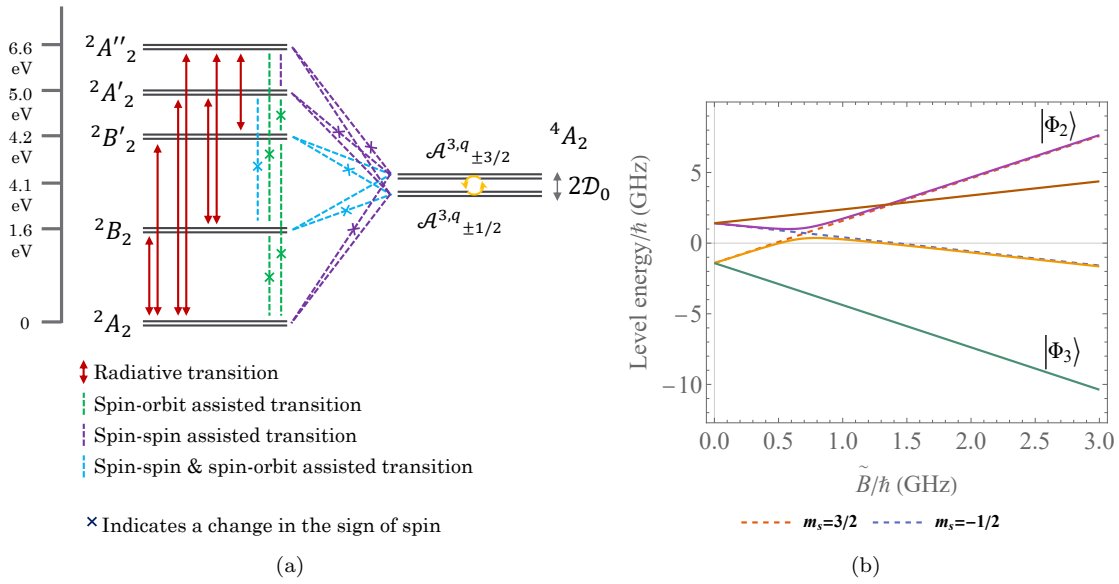

Figure 5.3: (a) The electronic structure of the C_2C_N defect and possible radiative and nonradiative transitions. Red lines shows the possible electric-dipole transitions. While dashed lines indicate possible phonon-assisted transitions. Yellow arrows show mixing between $A^{(3,q)}_{\pm 1/2}$ and $A^{(3,q)}_{\pm 3/2}$ due to the spin-spin coupling. The spin-spin coupling splits $^4A_2$ states by $2\mathcal{D}_0$ if we assume that $\mathcal{E}_3$ is much smaller than $\mathcal{D}_0$. The relative energy spacings of these states were obtained by our DFT calculations, which considers the Coulomb interaction and the HSE06 exchange-correlation functional. In this figure, we have assumed the quartet state is further detuned from the doublets than the spin-orbit coefficient. Usually the spin-orbit coefficient is on the order of GHz [3] and here the closest doublet to the quartet is separated by 0.1 eV corresponding to 24 THz. (b) The quartet-state anticrossing, which shows an anticrossing between the $|\Phi_1\rangle$ and $|\Phi_2\rangle$ states near $\tilde{B}_y/\hbar = 0.7\,\text{GHz}$. Here, we have assumed that $\tilde{\mathcal{D}}_0$ and $\tilde{\mathcal{E}}_3$ are equal to 1 GHz. The dashed lines show the behavior of states with $m_s = 3/2$ and $m_s = -1/2$ in the presence of a magnetic field.

5.7 Selection rules

Here we look at the dominant transition allowed by the interaction of the electron with the electromagnetic field, which is the electric dipole transition. The electric dipole interaction is defined as

$$H_{\text{dipole}} = \boldsymbol{E} \cdot \boldsymbol{d} = \sum_k e\boldsymbol{E} \cdot \boldsymbol{r}_k, \tag{5.9}$$

where $\boldsymbol{E}$ is the electric field, $\boldsymbol{d}$ is the electric dipole moment, $\boldsymbol{r}_k$ is the position of k electron with respect to the nucleus, and e is the elementary electric charge. The position $\boldsymbol{r}$ in the C_{2v} group transforms like (B_1, B_2, A_1). Thus, according to Table 5.3, the allowed transitions are induced by either $eE_x x$ or $eE_z z$ and the dipole moment lies completely in the plane. The dipole allowed transitions and the matrix elements are given in the appendix (Sec. A.3). These results are summarized in Fig. 5.3(a), which shows radiative and nonradiative transitions along with the energy levels of the states.

5.8 External magnetic field

In the presence of an external magnetic field, there will be another term for the Zeeman interaction of the magnetic field with spin and orbital angular momentum [3]. This interaction is given by

$$H_{\mathrm{B}} = \frac{e}{2m_{\mathrm{e}}} \sum_k (\boldsymbol{l}_k + g_{\mathrm{e}} \boldsymbol{s}_k) \cdot \boldsymbol{B}, \tag{5.10}$$

where g_{e} is the electron-spin g factor, $\boldsymbol{s}$ is the electron spin, $\boldsymbol{l}$ is electron orbital angular momentum, $\boldsymbol{B}$ is the external magnetic field, and k sums over all electrons. But since l_z transforms as IR A_2 and l_x transforms as IR B_2, according to Table 5.3, they do not contribute to the Hamiltonian. Therefore, the Zeeman interaction will be simplified to $H_{\mathrm{B}} = \frac{e}{2m_{\mathrm{e}}} \sum_k (B_x g_{\mathrm{e}} s_{x,k} + B_y (l_{y,k} + g_{\mathrm{e}} s_{y,k}) + B_z g_{\mathrm{e}} s_{z,k})$. The matrix elements of the Hamiltonian above are given in Appendix.

5.8.1 Quartet state anticrossing

As we discussed previously, the spin-spin interaction splits and mixes the quartet-state eigenvalues and the spin-orbit interaction does not affect them. Adding a magnetic field perpendicular to the h-BN sheet ($\hat{y}$), modifies the energy eigenvalues of the quartet state. We add the matrix elements of the interactions for the quartet state from preceding sections and find its eigensystem. The energy eigenvalues are given by

$$\begin{aligned} E_1 &= \tilde{B}_y - \kappa_1, \\ E_2 &= \tilde{B}_y + \kappa_1, \\ E_3 &= -\tilde{B}_y - \kappa_1, \\ E_4 &= -\tilde{B}_y + \kappa_1, \end{aligned} \tag{5.11}$$

and eigenvectors are given by

$$
\begin{aligned}
|\Phi_1\rangle \quad &= \mu_1 |\mathcal{A}^{3,q}_{-1/2}\rangle + i\mu_1 |\mathcal{A}^{3,q}_{+1/2}\rangle \\
&\quad +i |\mathcal{A}^{3,q}_{-3/2}\rangle + |\mathcal{A}^{3,q}_{+3/2}\rangle , \\
|\Phi_2\rangle \quad &= -\mu_2 |\mathcal{A}^{3,q}_{-1/2}\rangle - i\mu_2 |\mathcal{A}^{3,q}_{+1/2}\rangle \\
&\quad +i |\mathcal{A}^{3,q}_{-3/2}\rangle + |\mathcal{A}^{3,q}_{+3/2}\rangle , \\
|\Phi_3\rangle \quad &= -\nu_1 |\mathcal{A}^{3,q}_{-1/2}\rangle + i\nu_1 |\mathcal{A}^{3,q}_{+1/2}\rangle \\
&\quad -i |\mathcal{A}^{3,q}_{-3/2}\rangle + |\mathcal{A}^{3,q}_{+3/2}\rangle , \\
|\Phi_4\rangle \quad &= -\nu_2 |\mathcal{A}^{3,q}_{-1/2}\rangle + i\nu_2 |\mathcal{A}^{3,q}_{+1/2}\rangle \\
&\quad -i |\mathcal{A}^{3,q}_{-3/2}\rangle + |\mathcal{A}^{3,q}_{+3/2}\rangle ,
\end{aligned}
\tag{5.12}
$$

where the coefficients are defined as

$$
\begin{aligned}
\kappa_1 &= \sqrt{4\tilde{B}_y^2 + \tilde{\mathcal{D}}_0^2 + \tilde{\mathcal{E}}_3^2 - 2\tilde{B}_y\left(\tilde{\mathcal{D}}_0 + \sqrt{3}\tilde{\mathcal{E}}_3\right)}, \\
\kappa_2 &= \sqrt{4\tilde{B}_y^2 + \tilde{\mathcal{D}}_0^2 + \tilde{\mathcal{E}}_3^2 + 2\tilde{B}_y\left(\tilde{\mathcal{D}}_0 + \sqrt{3}\tilde{\mathcal{E}}_3\right)}, \\
\mu_1 &= \frac{\left(\sqrt{3}\tilde{B}_y + \tilde{\mathcal{E}}_3\right)\left(\kappa_1 - \tilde{B}_y + \tilde{\mathcal{D}}_0\right)}{3\tilde{B}_y^2 - \tilde{\mathcal{E}}_3^2}, \\
\mu_2 &= \frac{\left(\sqrt{3}\tilde{B}_y + \tilde{\mathcal{E}}_3\right)\left(\kappa_1 + \tilde{B}_y - \tilde{\mathcal{D}}_0\right)}{3\tilde{B}_y^2 - \tilde{\mathcal{E}}_3^2}, \\
\nu_1 &= \frac{\left(\sqrt{3}\tilde{B}_y - \tilde{\mathcal{E}}_3\right)\left(\kappa_2 + \tilde{B}_y + \tilde{\mathcal{D}}_0\right)}{3\tilde{B}_y^2 - \tilde{\mathcal{E}}_3^2}, \\
\nu_2 &= \frac{\left(\tilde{\mathcal{E}}_3 - \sqrt{3}\tilde{B}_y\right)\left(-\kappa_2 + \tilde{B}_y + \tilde{\mathcal{D}}_0\right)}{\tilde{\mathcal{E}}_3^2 - 3\tilde{B}_y^2}.
\end{aligned}
\tag{5.13}
$$

The variables with tildes are defined below to simplify the equations.

$$
\begin{aligned}
\tilde{B}_y &= \frac{\gamma_e \hbar}{2} B_y \\
\tilde{\mathcal{D}}_0 &= \frac{\mu_0 \gamma_e^2 \hbar^2}{16\pi} \mathcal{D}_0 \\
\tilde{\mathcal{E}}_3 &= \frac{\mu_0 \gamma_e^2 \hbar^2}{16\pi} \mathcal{E}_3
\end{aligned}
\tag{5.14}
$$

Based on these results and as shown in Fig. 5.3(b), an anticrossing happens between $|\Phi_1\rangle$ and $|\Phi_2\rangle$ when the magnetic field compensates the spin-spin splitting at $\tilde{B}_y$ near $(\tilde{\mathcal{D}}_0^2 + \tilde{\mathcal{E}}_3^2)^{1/2}\big/2$. The $|\Phi_3\rangle$ state remains

unmixed as it is diverging from other states. The $|\Phi_4\rangle$ state is not mixed too, despite the fact that the $|\Phi_2\rangle$ state passes it at $\tilde{B}_y$ near $(\tilde{\mathcal{D}}_0^2 + \tilde{\mathcal{E}}_3^2)^{1/2}$.

5.9 Ground-state hyperfine interaction

Nuclear spins in solids are a promising candidate for storing information and using them as quantum memories due to their long coherence time [118]. Nuclear-spin quantum memories have been demonstrated experimentally for the orbital ground state of the negatively-charged nitrogen-vacancy center in diamond [119, 120]. In this section, we investigate the effect of the presence of a carbon-13 nuclear spin in the defect, which is given by $\hat{\tilde{H}} = \hat{H}_{13\mathrm{C}} + \hat{V}_{\mathrm{mhf}} + \hat{V}_{\mathrm{ehf}}$. The first term is the Zeeman interaction of the nuclear spin with an external magnetic field, which is given by $\hat{H}_{13\mathrm{C}} = -\gamma_{13\mathrm{C}} \boldsymbol{B} \cdot \hat{\boldsymbol{I}}$, where $\hat{\boldsymbol{I}}$ is the nuclear spin and $\gamma_{13\mathrm{C}}$ is the nuclear-spin gyromagnetic ratio of ^{13}C. The second (third) term is the electric (magnetic) component of the hyperfine interaction of the ground electronic state of the defect with the ^{13}C nuclear spin [121, 83]. We only have to look at the magnetic component since ^{13}C has a nuclear spin of $I = 1/2$, and the electric component is due to the quadrupole moment of nuclei with spin $I \geq 1$ [122]. Also, we ignored the nuclear spin-spin interactions in this paper.

The magnetic hyperfine Hamiltonian accounts for the interaction between the nuclear spin and the electronic orbital magnetic moment in addition to the dipole-dipole interaction between the nuclear spin and the electron spin. The component of the hyperfine interaction that is related to the orbital angular momentum is given by $2 g_I \mu_N \mu_B \frac{\mu_0 \hbar}{4\pi} \sum_i \frac{1}{r_{i\mathrm{C}}^3} \boldsymbol{I} \cdot \boldsymbol{L}$, where μ_N is the nuclear magneton, μ_B is the Bohr magneton, g_I is the nuclear g-factor, and $r_{i\mathrm{C}}$ is the distance between ^{13}C and electron i. This component is zero based on Table 5.3, since our ground states transform as IR B_2 and do not have orbital angular momentum. Hence, we only need to consider the dipole-dipole interaction between the electron spin and the nuclear spin. The magnetic part of the hyperfine Hamiltonian, with these considerations, is given by

$$\begin{aligned} \hat{V}_{\mathrm{mhf}} &= C_{\mathrm{mhf}} \sum_i \left\{ \left(\frac{8\pi}{3} \delta(\hat{r}_{i\mathrm{C}}) - \frac{1}{r_{i\mathrm{C}}^3} \right) \hat{s}_i \cdot \hat{I} \right. \\ &\qquad \left. + \frac{3(\hat{s}_i \cdot \hat{r}_{i\mathrm{C}})(\hat{I} \cdot \hat{r}_{i\mathrm{C}})}{r_{i\mathrm{C}}^5} \right\} \\ &= -C_{\mathrm{mhf}} \sum_i \hat{s}_i \cdot \hat{A}_i^{(2)} \cdot \hat{I} \\ &= -C_{\mathrm{mhf}} \sum_i [\hat{J}_i^{(2)} \otimes \hat{A}_i^{(2)}]^{(0)}, \end{aligned} \tag{5.15}$$

where $C_{\text{mhf}} = g_I \mu_N g_e \mu_B \frac{\mu_0 \hbar^2}{4\pi}$, and $\hat{A}_i^{(2)}$ is a second rank tensor. The Fermi contact term contributes to the energy of orbitals with nonzero value of the wave function at the position of the nucleus. However, based on our DFT calculations [Fig. 5.2(a)], the wave functions are zero at the position of the carbon nuclei and we can ignore the Dirac delta term. Consequently, the second-order tensor $\hat{A}_i^{(2)}$ is given by

$$\hat{A}_i^{(2)} = \frac{1}{r_{i\text{C}}^5} \begin{pmatrix} r_{i\text{C}}^2 - 3x_{i\text{C}}^2 & -3x_{i\text{C}}y_{i\text{C}} & -3x_{i\text{C}}z_{i\text{C}} \\ -3x_{i\text{C}}y_{i\text{C}} & r_{i\text{C}}^2 - 3y_{i\text{C}}^2 & -3y_{i\text{C}}z_{i\text{C}} \\ -3x_{i\text{C}}z_{i\text{C}} & -3y_{i\text{C}}z_{i\text{C}} & r_{i\text{C}}^2 - 3z_{i\text{C}}^2 \end{pmatrix}. \tag{5.16}$$

For simplifying further calculations, we define $\hat{J}_j^{(2)} = \hat{s}_i \otimes \hat{I}$ and write the interaction in the compound tensor form.

According to Table 5.3, for the ground states $|\mathcal{A}_{\pm 1/2}^{0,d}\rangle$, only the operators of the form O^{A_1} contributes to the hyperfine interaction. Thus, only the diagonal terms of $\hat{A}_i^{(2)}$ in Eq. (5.16) transform as IR A_1 contribute to the hyperfine interaction of the ground state, and the off-diagonal terms do not contribute. We write the basis of the ground state of the defect coupled to a ^{13}C nuclear spin as

$$\begin{aligned} |\Psi_1^g; 1, +1\rangle &= |\mathcal{A}_{+1/2}^{0,d}\rangle\, |+\rangle_I, \\ |\Psi_2^g; 1, 0\rangle &= \frac{1}{\sqrt{2}}(|\mathcal{A}_{+1/2}^{0,d}\rangle\, |-\rangle_I + |\mathcal{A}_{-1/2}^{0,d}\rangle\, |+\rangle_I), \\ |\Psi_3^g; 1, -1\rangle &= |\mathcal{A}_{-1/2}^{0,d}\rangle\, |-\rangle_I, \\ |\Psi_4^g; 0, 0\rangle &= \frac{1}{\sqrt{2}}(|\mathcal{A}_{+1/2}^{0,d}\rangle\, |-\rangle_I - |\mathcal{A}_{-1/2}^{0,d}\rangle\, |+\rangle_I). \end{aligned} \tag{5.17}$$

Based on the symmetry of the system, there can only be nonzero hyperfine matrix elements for states that have $\Delta S \in \{0, \pm 2\}$. The results of the calculations for matrix elements are shown in the appendix [Sec. C].

5.10 Transition rates

Here we show our results for the radiative and the electron-phonon induced nonradiative transition rates between the $\{^2A_2, ^2B_2, ^2B_2'\}$ doublet states. The results of the calculations are presented in the following sections.

5.10.1 Radiative rates

The radiative transitions occur at a rate given by

$$\Gamma_{\text{rad}} = \frac{1}{\tau_{\text{rad}}} = \frac{nE_{\text{ZPL}}^3\mu^2}{3\pi\epsilon_0 c^3\hbar^4}, \tag{5.18}$$

where n is the refractive index of h-BN, E_{ZPL} is the zero-phonon transition energy, μ is the transition dipole moment, and ϵ_0 is the vacuum permittivity [123, 124]. The refractive index of h-BN is taken to be $n = 2.1$ [125]. Equation (5.18) was evaluated for the ${}^2B_2 \rightarrow {}^2A_2$ and ${}^2B_2' \rightarrow {}^2A_2$ transitions, which amounts to calculating the corresponding transition dipole moments. The `wfck2r.x` module in QUANTUM ESPRESSO was used to produce the spin-polarized, real-space wave functions, from which the transition dipole moments were directly computed. Table 5.4 summarizes the results.

Transition	$\boldsymbol{\mu}$	μ [eÅ]	E_{ZPL} [eV]	τ_{rad} [ns]	Γ_{rad} [MHz]
${}^2B_2 \rightarrow {}^2A_2$	$\langle a_\downarrow \vert e\boldsymbol{r} \vert b_\downarrow \rangle$	0.68	1.6	64.5	15.5
${}^2B_2' \rightarrow {}^2A_2$	$\langle b_\uparrow' \vert e\boldsymbol{r} \vert a_\uparrow \rangle$	0.11	4.2	144.4	6.9

Table 5.4: Lifetimes, τ_{rad}, and rates, Γ_{rad}, of the radiative transitions used in our ODMR simulation.

5.10.2 Nonradiative rates

The nonradiative rates due to electron-phonon coupling can be calculated within the static coupling and one-dimensional effective phonon approximations [126, 127]. The nonradiative transition rate between an initial electron state i and a final electron state f is given by

$$\Gamma_{\text{nr}} = \frac{1}{\tau_{\text{nr}}} = \frac{2\pi}{\hbar} g |W_{if}|^2 X_{if}, \tag{5.19}$$

where g is the degeneracy of the final state. Equation (5.19) includes contributions from a phonon term, X_{if}, and an electronic term, W_{if}. The phonon term is given by

$$X_{if} = \sum_{n,m} p_{in} |\langle \chi_{fm} | Q - Q_0 | \chi_{in} \rangle|^2 \delta(E_{\text{ZPL}} + m\hbar\Omega_f - n\hbar\Omega_i), \tag{5.20}$$

where Q is the generalized coordinate defined in Ref. [126], and Q_0 is taken to be the relaxed atomic coordinates of the final electronic state ($\boldsymbol{R}_0$). Here, p_{in} is the thermal occupation of the phonon state n in the electronic state i, $|\chi_{jk}\rangle$ is the phonon wave function of the phonon state k in the electronic state j, and $\hbar\Omega_{\{i,f\}}$ are the effective phonon energies of the initial and final states. The phonon overlap can be calculated

directly using the quantum harmonic-oscillator wave functions. The electronic term is given by

$$W_{if} = \langle \psi_i(\boldsymbol{r}, \boldsymbol{R}) | \frac{\partial H}{\partial Q} | \psi_f(\boldsymbol{r}, \boldsymbol{R}) \rangle \, |_{\boldsymbol{R}=\boldsymbol{R}_0}, \tag{5.21}$$

which can be calculated numerically by finite differences using the DFT single-particle wave functions at the Γ-point [126, 128]. The nonradiative rates for the ${}^2B_2 \rightarrow {}^2A_2$ and ${}^2B_2' \rightarrow {}^2A_2$ transitions were computed by modifying the open-source `Nonrad` code [128]. The results are summarized in Table 5.5, which shows that the nonradiative rates are negligible compared with the radiative rates. The nonradiative ${}^2B_2' \rightarrow {}^2B_2$ transition is a second-order two-phonon process, and as such, it should occur at a much slower rate than the already negligible nonradiative rates.

Transition	E_{ZPL} [eV]	ΔQ [amu$^{1/2}$Å]	$\hbar\omega_i$ [meV]	$\hbar\omega_f$ [meV]	S_f	X_{if} [amu Å^2 eV^{-1}]	W_{if} [eV amu$^{-1/2}$ Å^{-1}]	τ_{nr} [ms]	Γ_{nr} [kHz]
${}^2B_2 \rightarrow {}^2A_2$	1.6	0.36	95.7	95.4	1.49	3.66×10^{-11}	5.40×10^{-2}	0.5	2
${}^2B_2' \rightarrow {}^2A_2$	4.2	0.21	91.8	94.9	0.52	2.31×10^{-20}	3.55×10^{-1}	$> 10^3$	$< 10^{-3}$

Table 5.5: Nonradiative recombination properties within the static coupling and one-dimensional effective phonon approximations, evaluated at 300 K. The relaxed atomic coordinates of the ground state are set to $Q_0 = 0$, from which the excited-state equilibrium coordinates are offset by ΔQ. For completeness, we have included the ground-state Huang-Rhys factor which quantifies the strength of the electron-phonon coupling, as computed in the one-dimensional approximation, $S_f = (\Delta Q)^2 \Omega_f / 2\hbar$.

An approach to calculate the intersystem crossing rate was developed by Smart et al. [129], which requires the spin-orbit coupling strength and the phonon overlap, but calculating the nonradiative rates for the intersystem crossing transitions is beyond the scope of this paper.

5.11 ODMR signal

There have been reports of ODMR signals for defects in h-BN. One of them is known to originate from the V_B^- defect [111], while the origins of the other observed ODMR signals are not established yet [112, 4]. Here, we present our results for the ODMR simulation using the model in Fig. 5.4 for the C_2C_N defect. We used the Lindblad master equation to derive the second-order correlation function $g^{(2)}$ and the ODMR contrast.

The Lindblad master equation is defined as

$$\begin{aligned} \frac{d}{dt}\rho &= \mathcal{L}\rho \\ &\equiv -i[H, \rho] + \sum_k \Gamma_k \left(L_k \rho L_k^\dagger - \frac{1}{2}\{L_k L_k^\dagger, \rho\} \right), \end{aligned} \tag{5.22}$$

where $\mathcal{L}$ is the Liouvillian superoperator [92]. The first term of $\mathcal{L}$ gives the unitary time evolution of the density matrix, ρ, and the other terms are responsible for the transitions of the system. The operators L_k are called jump operators, and the constants Γ_k are the transition rates. We have used three types of jump operators in our simulation, including operators for optical, nonradiative, and spin transitions.

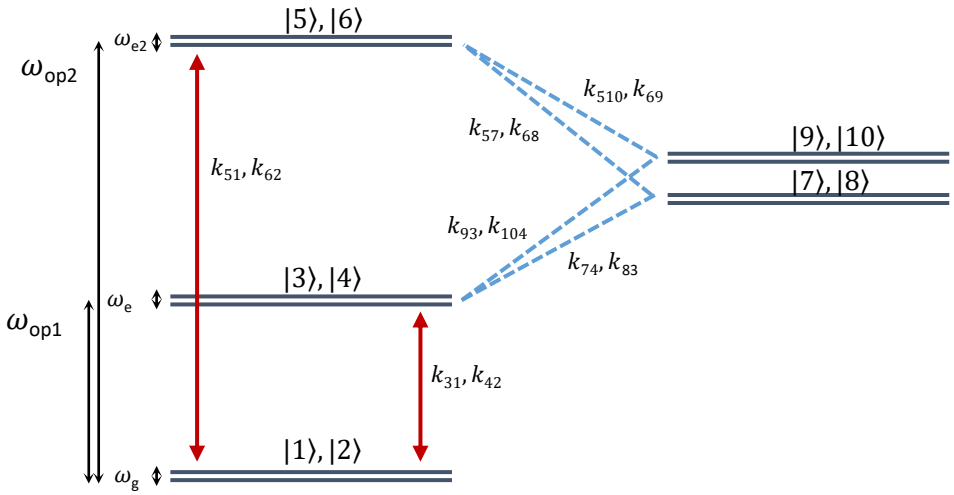

Figure 5.4: Our model for ODMR simulation. In this model, the energy spacing between levels, denoted by ω_{op1} and ω_{op2}, and optical rates, denoted by the red arrows, are based on DFT calculations and nonradiative rates to and from the metastable states, denoted by blue dashed lines, are approximated by rates from other studies on defects in h-BN. There are also spin splittings due to the external magnetic field, which are denoted by ω_g, ω_e, and ω_{e2}. According to the matrix elements of the spin-orbit and spin-spin interactions of this defect, the dashed lines are spin-dependent transitions which are vital for observing an ODMR signal.

We simulate a coherent laser pulse to excite the ground doublet state $\{|1\rangle, |2\rangle\}$ to one of the two excited doublet states $\{|3\rangle, |4\rangle\}$ or $\{|5\rangle, |6\rangle\}$. All of these electronic states are spin 1/2 states, and their spin states are split due to an external magnetic field. We also simulate a coherent microwave pulse to probe the ODMR signal by changing its energy around the spin-splitting energy.

If the quartet dark states $\{|7\rangle, |8\rangle, |9\rangle, |10\rangle\}$ do not overlap with the phonon sideband of the first excited states $\{|3\rangle, |4\rangle\}$, they can act as a metastable manifold during the decay of the second excited states $\{|5\rangle, |6\rangle\}$. Since we predict that the quartet energy of around 4.1 eV is far above the 1.6 eV of the first excited doublet, it is unlikely that there is an overlap with the phonon sideband, which is typically smaller than about 500 meV for defects in h-BN [80]. In addition, the decay to the quartet state and from the quartet state to the first excited state can depend on the spin, and hence the system could produce an ODMR signal. To see this signal, one should excite the ground-state levels to the second excited state doublet $\{|5\rangle, |6\rangle\}$, after which a spin-dependent nonradiative transition can occur into the quartet manifold.

The ${}^2B_2'$ state is the most promising candidate for photoexcitation because its energy is very close to the quartet state, and most likely, it will overlap with its phonon sideband, allowing for fast nonradiative

transitions to the metastable state. Thus, we restricted the model to the ${}^2B_2'$ level and ignored ${}^2A_2'$ and ${}^2A_2''$ levels because of their high energy. We also ignored nonradiative transitions related to ${}^2B_2' \leftrightarrow {}^2A_2$, ${}^2B_2 \leftrightarrow {}^2A_2$, and ${}^4A_2 \leftrightarrow {}^2A_2$ because the energy difference between them is large and it is more likely that the radiative and intersystem crossing transitions will be dominant. Consequently, we need an ultraviolet (UV) laser pulse to excite the ground doublet state to the second excited doublet state. Finally, we detect photons emitted due to the decay of electrons from the second doublet excited state, $\{|5\rangle, |6\rangle\}$, to the ground state, $\{|1\rangle, |2\rangle\}$. UV lasers and detectors will be required to verify our predictions. The equipment and techniques used in ion trap systems could be helpful since some of the ions used in the ion trap systems have a transition in the UV regime, for example, Be+ (3.96 eV) or Mg+ (4.43 eV) [130, 131, 132].

parameter	value	parameter	value
ω_{op2}	4.20 eV	ω_{op1}	1.60 eV
Ω_{op}	7 MHz	Ω_{MW}	13 MHz
k_{51}	6.9 MHz	k_{62}	6.9 MHz
k_{31}	15.5 MHz	k_{42}	15.5 MHz
k_{57}	0.1 MHz	k_{68}	1 MHz
k_{74}	2 MHz	k_{83}	1 MHz
k_{510}	0.95 MHz	k_{69}	0.045 MHz
k_{93}	1.1 MHz	k_{104}	0.11 MHz
ω_g	700 MHz	ω_{e2}	697 MHz
ω_e	703 MHz	γ_{spin}	0.06 MHz

Table 5.6: Parameters used in the ODMR simulation. Ω_{op} is the coherent optical driving Rabi frequency, Ω_{MW} is the coherent microwave driving Rabi frequency, γ_{spin} is the spin relaxation rate, and other parameters are shown in Fig. 5.4.

The results obtained by exciting the ground-state levels directly to the second excited state and then detecting photon emissions from the same state to the ground state are given in Fig. 5.5. We have used the optical decay rates from our DFT calculation presented in the previous section. The intersystem crossing rates, metastable decay rates, and spin-relaxation rates for which we see ODMR signal are on the order of magnitude of the rates seen in other defects [133, 134], but more calculations are needed to verify if the rates are in the proper range for the C_2C_N defect. In our simulation, we chose the optical Rabi frequency close to the saturation point so that it is not in the resonance regime (Fig. 5.6). Additionally, the microwave Rabi frequency was chosen such that the ODMR signal had the highest value (Fig. 5.7). All the parameters used to predict this ODMR signal are given in Table 5.6.

Some of the parameters used for this simulation were not calculated by *ab initio* calculations. Hence, we probe a bigger space of possible values, keeping the rates close to the rates seen for other defects in h-BN, in order to see how the ODMR signal would change. Varying the parameters used for this model shows that the difference between k_{74} and k_{83} is essential for having an ODMR signal. Based on our calculations for the spin-orbit and the spin-spin interactions, the matrix elements responsible for these transitions are different

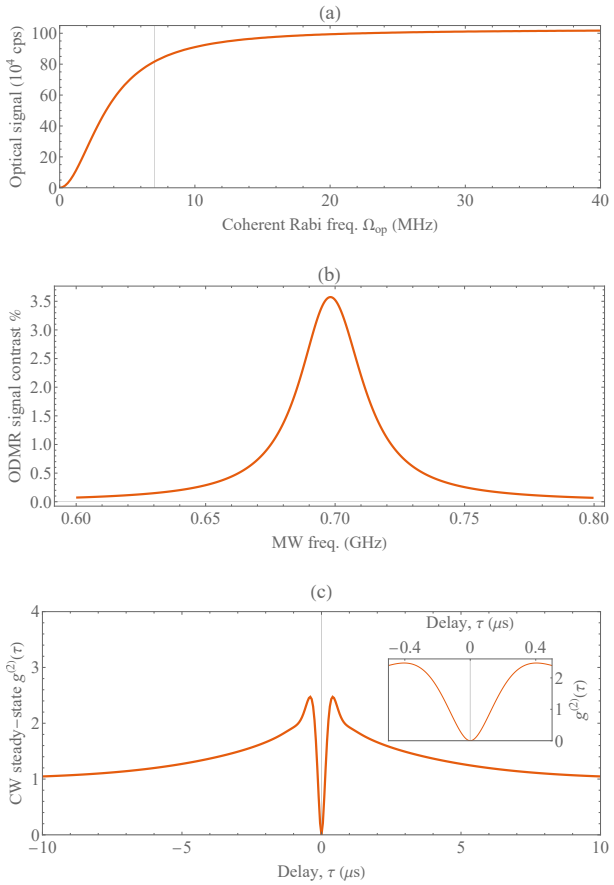

Figure 5.5: Results of exciting photons to the second excited doublet state and detecting photon emissions from the same state to the ground state. (a) Optical signal versus coherent Rabi frequency, which shows saturation near 20 MHz. The grid line shows the Rabi frequency that we used for the ODMR signal and the g^2 function. This is the frequency where the optical signal is near 80 % of the saturation point. (b) The ODMR signal, which shows 3.5 % contrast at 700 MHz MW frequency. (c) The second-order correlation function, which shows significant bunching at microsecond timescales due to the metastable quartet state, and antibunching pattern at $\tau = 0$. Inset shows the same g^2 function for smaller timescales.

for the spin up and down. The transition amplitudes are proportional to these matrix elements, allowing the defect to have spin-dependent decay rates from and to the quartet state. The effect of changing k_{74} and k_{83} on the ODMR signal and g^2 correlation function is shown in Fig. 5.8. Based on the matrix elements of the spin-orbit and spin-spin interactions, the k_{74} and k_{83} rates are related to the k_{93} and k_{104} rates. So changing each of them will affect the other two. More figures are provided in the appendix Sec. E. These results show that even for the bigger space of possible transition rates, the ODMR signal of a few percent is viable.

The calculated linewidth of the ODMR signal is due only to the natural or lifetime broadening since we have not included other broadening mechanisms such as the hyperfine interaction in our simulation. However, the most abundant isotopes of nitrogen and boron have nuclear spins of 1 and 3/2, respectively.

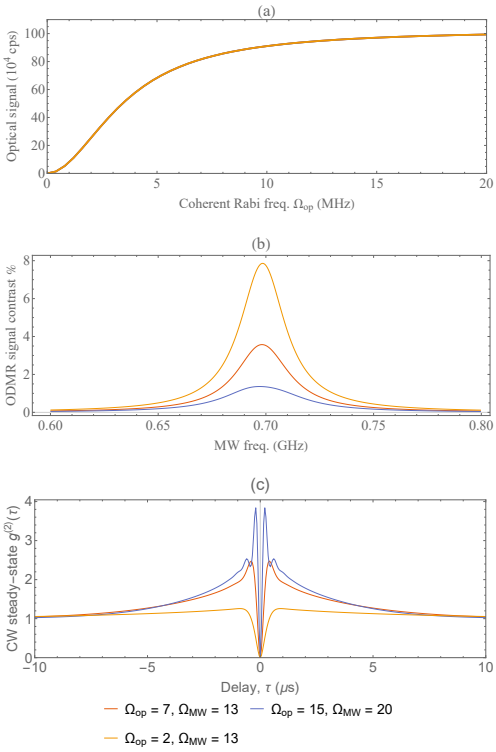

Figure 5.6: The effect of changing Ω_{op} on the optical signal, ODMR contrast, and the second-order correlation function. All the variables are in MHz. When the optical Rabi frequency is in the saturation region, e. g. $\Omega_{op} = 15\,\text{MHz}$, there are oscillations in the $g^2(\tau)$ function. This might be related to the oscillations seen by Stern et al. [4].

It has been shown that the hyperfine interaction of the surrounding nuclear spins has a considerable effect on the ODMR linewidth broadening of defects in h-BN (51 MHz for the C_2C_N defect) [89]. As it can be seen in Fig. 5.8, the linewidth of the ODMR signal due to the natural broadening changes significantly for different nonradiative transition rates, which are still unknown. Therefore, after finding the correct value of the transition rates, it will be crucial to consider hyperfine broadening, because the linewidth of the ODMR signal is another parameter that helps identify defects found by the experiment.

5.12 Computational details

The DFT calculations and post-processing were performed using the QUANTUM ESPRESSO open-source software package [135]. The calculations utilized a plane-wave basis set with a kinetic-energy cutoff of 350 eV and projector augmented-wave pseudopotentials [136]. All relaxation calculations were performed with a force convergence threshold of $10^{-4}\,\text{eV/Å}$. Experimental investigations of point defects in h-BN typically consider multilayer samples; however, it has been shown that DFT calculations result in negligible differences between the electronic structure of defects in single- and multilayer systems [68]. Our supercell consists

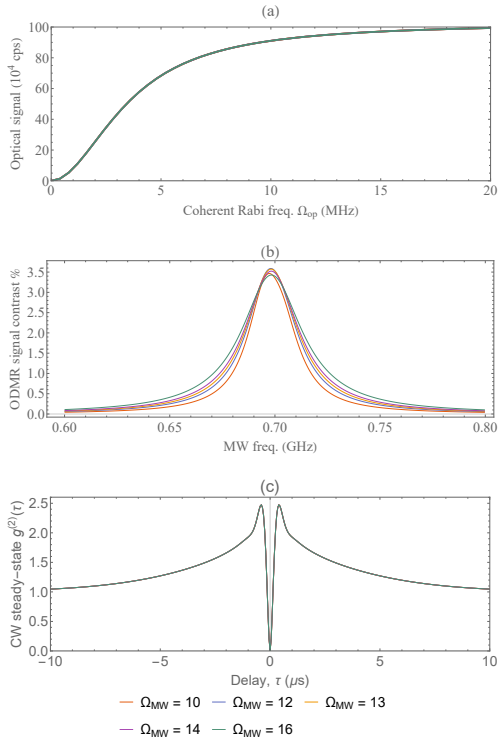

Figure 5.7: The effect of changing Ω_{MW} on the optical signal, ODMR contrast, and the second-order correlation function. All the variables are in MHz. It is important to choose Ω_{MW} in a way that the ODMR signal is maximum.

of 98 atoms and a vacuum separation of 15 Å between layers, corresponding to 7×7 unit cells of mono-layer h-BN. The atomic positions and in-plane lattice constant for the pristine h-BN structure were relaxed using the Perdew-Burke-Ernzerhof (PBE) exchange-correlation functional [137]. An in-plane lattice constant of $a = 2.5$ Å was obtained, consistent with previous findings [138]. The Heyd-Scuseria-Ernzerhof (HSE) hybrid functional [139] was then used to optimize the direct bandgap at the K high-symmetry point [140] to the bulk value of ≈ 6 eV [81]. A bandgap of 5.98 eV was obtained by setting the mixing parameter to 0.32 and fine-tuning the screening parameter to 0.086 Å^{-1}.

The C_2C_N defect was then added to the hexagonal lattice, the atomic positions were relaxed in-plane, and the ground-state wave functions of the single-particle defect levels were calculated. Next, the single-configuration excited states ($^2A_2$, $^2B_2$, $^2B_2'$, and $^4A_2$) were created using the ΔSCF method [141], and the atomic positions of each excited-state electronic configuration were relaxed in-plane. The transition energies between defect states were calculated by considering the difference in total energies of the structures, obtained via spin-polarized calculations performed within the Γ-point approximation. The HSE06 functional has been shown to provide accurate results for defects in h-BN which exhibit low correlation and charge transfer, and as such, it is expected that the error in the DFT calculations of the single-configuration states is on the

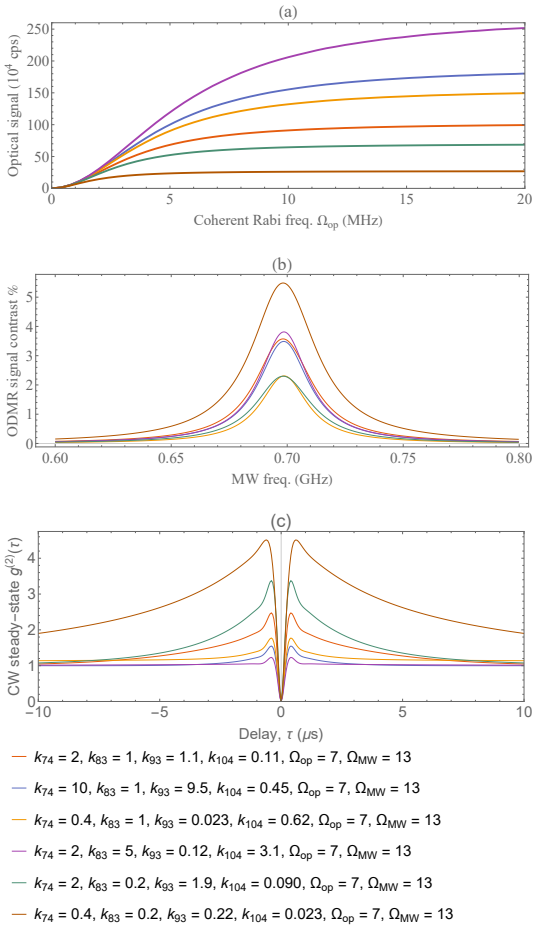

Figure 5.8: The effect of changing k_{83} and k_{74} on the optical signal, ODMR contrast, and the second-order correlation function. All the variables are in MHz.

order of 0.1 eV [142, 87]. The remaining states of interest ($^2A_2'$ and $^2A_2''$) are multiconfiguration states which cannot be modeled in the DFT calculations using the ΔSCF method. Rough estimates for the corresponding transitions energies were obtained following the method of Ref. [143, 123], making use of the single-configuration states $|bab'\rangle$, $|ba\overline{b'}\rangle$, and $|b\overline{a}b'\rangle$ which were created within the ΔSCF procedure (see appendix Sec. D for detailed calculations).

Reference [144] investigates the C_2C_N defect. A difference between this work and Ref. [144] can be seen in the positioning of the single-electron states with respect to the conduction and valence bands. The electronic calculations of Ref. [144] were performed within the GW approximation, which can impact both the position and size of the bandgap. We note, however, that relative spacing and positions of the defect state energies found in our work are consistent with the findings of both Refs. [87] and [89].

Chapter 6

Conclusion and outlook

We have used group theory and DFT calculations to find the electronic structure and transitions of the C_2C_N defect in 2D h-BN. The results are summarized in Fig. 5.3(a), which shows that there are several radiative transitions together with spin-orbit and spin-spin-assisted nonradiative transitions. Also, the spin-spin interaction causes a splitting between quartet states $^4A_2$. We studied the effect of an external magnetic field and found that, in the presence of an external magnetic field perpendicular to the plane, there is an anticrossing between the states of the quartet manifold. We also looked at the ground-state hyperfine interactions, which can be helpful in future studies. Additionally, we calculated the radiative rates and some of the nonradiative rates using DFT. Finally, we simulated the system using the Lindblad master equation. Although our results indicate that it is unlikely for the C_2C_N defect to be responsible for the ODMR signals that have been reported so far, we show that it could be possible to see an ODMR signal contrast of $\approx 3.5\%$ for the configuration discussed in the text. Some of the nonradiative rates of the C_2C_N are unknown. Hence, we looked at the ODMR signal in a subspace of the possible rates where these variables are close to the reported values from other defects in h-BN and show that an ODMR signal of a few percent is still viable. Besides the ODMR signal contrast, the ODMR linewidth would also help identify this defect in experimental data. Thus, in future research, it will be essential to determine both the unknown nonradiative rates and the hyperfine broadening, which has a significant effect. In conclusion, the properties of the defect that we considered are essential for future applications, e.g., for quantum networks and quantum sensing.

6.1 Future work

Recently, Stern et al. have reported an ODMR signal from a carbon-related defect in h-BN [4]. They observe positive and negative ODMR signals, indicating highly tunable internal rates. Additionally, their

below-saturation ODMR lineshape measurements and spin model simulation reveal that defects exhibit an angle-dependent doublet resonance, consistent with a $S > 1/2$ system with modest zero-field splitting. However, the ODMR lineshape shows that the results are well described by the S = 1 model. Their results show that the optical rates are one order of magnitude bigger than the radiative rates of the C_2C_N defect, indicating a bigger dipole moment for the defect.

They have measured 27 defects with a bright ODMR signal with a mean ZPL energy of around 590 nm (2.10 eV). According to M. Maciaszek et al. [145], the star defects, $C_N(C_B)_3$ and $C_B(C_N)_3$, are carbon-related, have energies in the correct range and more importantly are spin 1 defects. The former has a higher density which means it forms more frequently in the h-BN lattice. So, it might be reasonable to start with this defect. But this doesn't exclude the $C_B(C_N)_3$ defect.

The combination of group theory and DFT is a powerful tool for understanding the electronic structure of any interesting defect. Further, the addition of the ODMR simulation, if there is any, allows us to compare the theory and experiment better and identify defects responsible for different measurements. One can use the methods and tools presented in this thesis to study the star defects or any other promising defect in h-BN or other solid-state color centers, which will help identify the defect or defects responsible for the measured signals.

Finally, our work can be extended to understand the C_2C_N carbon trimer defect better. For example, more group theory and DFT calculations can be performed to understand the effect of strain and phononic modes of this defect. Also, the hyperfine coupling effect can be included in the ODMR simulation to have a more accurate comparison between theory and experiment.

Bibliography

[1] Omid Golami, Kenneth Sharman, Roohollah Ghobadi, Stephen C. Wein, Hadi Zadeh-Haghighi, Claudia Gomes da Rocha, Dennis R. Salahub, and Christoph Simon. *abinitio* and group theoretical study of properties of a carbon trimer defect in hexagonal boron nitride. *Phys. Rev. B*, 105:184101, May 2022. doi: 10.1103/PhysRevB.105.184101. URL https://link.aps.org/doi/10.1103/PhysRevB.105.184101.

[2] Koichi Momma and Fujio Izumi. Vesta 3 for three-dimensional visualization of crystal, volumetric and morphology data. *Journal of Applied Crystallography*, 44(6):1272–1276, 2011. URL http://scripts.iucr.org/cgi-bin/paper?S0021889811038970.

[3] M W Doherty, N B Manson, P Delaney, and L C L Hollenberg. The negatively charged nitrogen-vacancy centre in diamond: the electronic solution. *New Journal of Physics*, 13(2):025019, February 2011. doi: 10.1088/1367-2630/13/2/025019. URL https://doi.org/10.1088/1367-2630/13/2/025019.

[4] Hannah L. Stern, Qiushi Gu, John Jarman, Simone Eizagirre Barker, Noah Mendelson, Dipankar Chugh, Sam Schott, Hoe H. Tan, Henning Sirringhaus, Igor Aharonovich, and Mete Atatüre. Room-temperature optically detected magnetic resonance of single defects in hexagonal boron nitride. *Nature Communications*, 13(1), February 2022. doi: 10.1038/s41467-022-28169-z. URL https://doi.org/10.1038/s41467-022-28169-z.

[5] Charles H. Bennett and David P. DiVincenzo. Quantum information and computation. *Nature*, 404 (6775):247–255, March 2000. doi: 10.1038/35005001. URL https://doi.org/10.1038/35005001.

[6] P.W. Shor. Algorithms for quantum computation: discrete logarithms and factoring. In *Proceedings 35th Annual Symposium on Foundations of Computer Science*. IEEE Comput. Soc. Press, 1994. doi: 10.1109/sfcs.1994.365700. URL https://doi.org/10.1109/sfcs.1994.365700.

[7] T. D. Ladd, F. Jelezko, R. Laflamme, Y. Nakamura, C. Monroe, and J. L. O'Brien. Quan-

tum computers. *Nature*, 464(7285):45–53, March 2010. doi: 10.1038/nature08812. URL https://doi.org/10.1038/nature08812.

[8] Ronald Hanson and David D. Awschalom. Coherent manipulation of single spins in semiconductors. *Nature*, 453(7198):1043–1049, June 2008. doi: 10.1038/nature07129. URL https://doi.org/10.1038/nature07129.

[9] David D. Awschalom, Lee C. Bassett, Andrew S. Dzurak, Evelyn L. Hu, and Jason R. Petta. Quantum spintronics: Engineering and manipulating atom-like spins in semiconductors. *Science*, 339(6124):1174–1179, March 2013. doi: 10.1126/science.1231364. URL https://doi.org/10.1126/science.1231364.

[10] M. H. Devoret and R. J. Schoelkopf. Superconducting circuits for quantum information: An outlook. *Science*, 339(6124):1169–1174, March 2013. doi: 10.1126/science.1231930. URL https://doi.org/10.1126/science.1231930.

[11] C. Monroe and J. Kim. Scaling the ion trap quantum processor. *Science*, 339(6124):1164–1169, March 2013. doi: 10.1126/science.1231298. URL https://doi.org/10.1126/science.1231298.

[12] Ady Stern and Netanel H. Lindner. Topological quantum computation—from basic concepts to first experiments. *Science*, 339(6124):1179–1184, March 2013. doi: 10.1126/science.1231473. URL https://doi.org/10.1126/science.1231473.

[13] John Clarke and Frank K. Wilhelm. Superconducting quantum bits. *Nature*, 453(7198):1031–1042, June 2008. doi: 10.1038/nature07128. URL https://doi.org/10.1038/nature07128.

[14] Morten Kjaergaard, Mollie E. Schwartz, Jochen Braumüller, Philip Krantz, Joel I.-J. Wang, Simon Gustavsson, and William D. Oliver. Superconducting qubits: Current state of play. *Annual Review of Condensed Matter Physics*, 11(1):369–395, March 2020. doi: 10.1146/annurev-conmatphys-031119-050605. URL https://doi.org/10.1146/annurev-conmatphys-031119-050605.

[15] Christopher R. Monroe and David J. Wineland. Quantum computing with ions. *Scientific American*, 299(2):64–71, August 2008. doi: 10.1038/scientificamerican0808-64. URL https://doi.org/10.1038/scientificamerican0808-64.

[16] V. Mourik, K. Zuo, S. M. Frolov, S. R. Plissard, E. P. A. M. Bakkers, and L. P. Kouwenhoven. Signatures of majorana fermions in hybrid superconductor-semiconductor nanowire devices. *Science*, 336(6084):1003–1007, May 2012. doi: 10.1126/science.1222360. URL https://doi.org/10.1126/science.1222360.

[17] A.Yu. Kitaev. Fault-tolerant quantum computation by anyons. *Annals of Physics*, 303(1):2–30, January 2003. doi: 10.1016/s0003-4916(02)00018-0. URL https://doi.org/10.1016/s0003-4916(02)00018-0.

[18] Jeremy L. O'Brien, Akira Furusawa, and Jelena Vučković. Photonic quantum technologies. *Nature Photonics*, 3(12):687–695, December 2009. doi: 10.1038/nphoton.2009.229. URL https://doi.org/10.1038/nphoton.2009.229.

[19] Fulvio Flamini, Nicolò Spagnolo, and Fabio Sciarrino. Photonic quantum information processing: a review. *Reports on Progress in Physics*, 82(1):016001, November 2018. doi: 10.1088/1361-6633/aad5b2. URL https://doi.org/10.1088/1361-6633/aad5b2.

[20] Lov K. Grover. A fast quantum mechanical algorithm for database search. In *Proceedings of the twenty-eighth annual ACM symposium on Theory of computing - STOC '96*. ACM Press, 1996. doi: 10.1145/237814.237866. URL https://doi.org/10.1145/237814.237866.

[21] Michael A. Nielsen and Isaac L. Chuang. *Quantum Computation and Quantum Information: 10th Anniversary Edition*. Cambridge University Press, Cambridge, 2010. doi: 10.1017/CBO9780511976667. URL https://doi.org/10.1017/CBO9780511976667.

[22] Jeremy L. O'Brien. Optical quantum computing. *Science*, 318(5856):1567–1570, December 2007. doi: 10.1126/science.1142892. URL https://doi.org/10.1126/science.1142892.

[23] Dorit Aharonov. A simple proof that toffoli and hadamard are quantum universal, 2003. URL https://arxiv.org/abs/quant-ph/0301040.

[24] E. Knill, R. Laflamme, and G. J. Milburn. A scheme for efficient quantum computation with linear optics. *Nature*, 409(6816):46–52, January 2001. doi: 10.1038/35051009. URL https://doi.org/10.1038/35051009.

[25] Robert Raussendorf and Hans J. Briegel. A one-way quantum computer. *Physical Review Letters*, 86(22):5188–5191, May 2001. doi: 10.1103/physrevlett.86.5188. URL https://doi.org/10.1103/physrevlett.86.5188.

[26] N. Yoran and B. Reznik. Deterministic linear optics quantum computation with single photon qubits. *Physical Review Letters*, 91(3), July 2003. doi: 10.1103/physrevlett.91.037903. URL https://doi.org/10.1103/physrevlett.91.037903.

[27] Michael A. Nielsen. Optical quantum computation using cluster states. *Physical Review Letters*, 93 (4), July 2004. doi: 10.1103/physrevlett.93.040503. URL https://doi.org/10.1103/physrevlett.93.040503.

[28] Juan Ortigoso. Twelve years before the quantum no-cloning theorem. *American Journal of Physics*, 86(3):201–205, March 2018. doi: 10.1119/1.5021356. URL https://doi.org/10.1119/1.5021356.

[29] Nicolas Gisin, Grégoire Ribordy, Wolfgang Tittel, and Hugo Zbinden. Quantum cryptography. *Reviews of Modern Physics*, 74(1):145–195, March 2002. doi: 10.1103/revmodphys.74.145. URL https://doi.org/10.1103/revmodphys.74.145.

[30] Nicolas Gisin and Rob Thew. Quantum communication. *Nature Photonics*, 1(3):165–171, March 2007. doi: 10.1038/nphoton.2007.22. URL https://doi.org/10.1038/nphoton.2007.22.

[31] Won-Young Hwang. Quantum key distribution with high loss: Toward global secure communication. *Physical Review Letters*, 91(5), August 2003. doi: 10.1103/physrevlett.91.057901. URL https://doi.org/10.1103/physrevlett.91.057901.

[32] Nicolas Sangouard and Hugo Zbinden. What are single photons good for? *Journal of Modern Optics*, 59(17):1458–1464, October 2012. doi: 10.1080/09500340.2012.687500. URL https://doi.org/10.1080/09500340.2012.687500.

[33] Nicolas Gisin, Stefano Pironio, and Nicolas Sangouard. Proposal for implementing device-independent quantum key distribution based on a heralded qubit amplifier. *Physical Review Letters*, 105(7), August 2010. doi: 10.1103/physrevlett.105.070501. URL https://doi.org/10.1103/physrevlett.105.070501.

[34] Vittorio Giovannetti, Seth Lloyd, and Lorenzo Maccone. Quantum-enhanced measurements: Beating the standard quantum limit. *Science*, 306(5700):1330–1336, November 2004. doi: 10.1126/science.1104149. URL https://doi.org/10.1126/science.1104149.

[35] Christian Weedbrook, Stefano Pirandola, Raúl García-Patrón, Nicolas J. Cerf, Timothy C. Ralph, Jeffrey H. Shapiro, and Seth Lloyd. Gaussian quantum information. *Reviews of Modern Physics*, 84(2):621–669, May 2012. doi: 10.1103/revmodphys.84.621. URL https://doi.org/10.1103/revmodphys.84.621.

[36] S. Pirandola, B. R. Bardhan, T. Gehring, C. Weedbrook, and S. Lloyd. Advances in photonic quantum sensing. *Nature Photonics*, 12(12):724–733, November 2018. doi: 10.1038/s41566-018-0301-6. URL https://doi.org/10.1038/s41566-018-0301-6.

[37] Vittorio Giovannetti, Seth Lloyd, and Lorenzo Maccone. Quantum metrology. *Physical Review Letters*, 96(1), January 2006. doi: 10.1103/physrevlett.96.010401. URL https://doi.org/10.1103/physrevlett.96.010401.

[38] Hannah Clevenson, Matthew E. Trusheim, Carson Teale, Tim Schröder, Danielle Braje, and Dirk Englund. Broadband magnetometry and temperature sensing with a light-trapping diamond waveguide. *Nature Physics*, 11(5):393–397, April 2015. doi: 10.1038/nphys3291. URL https://doi.org/10.1038/nphys3291.

[39] Rodney Van Meter. *Quantum networking*. Networks and telecommunications series. Iste Wiley, London Hobokem, NJ, 2014. ISBN 9781118648919.

[40] H. J. Kimble. The quantum internet. *Nature*, 453(7198):1023–1030, June 2008. doi: 10.1038/nature07127. URL https://doi.org/10.1038/nature07127.

[41] Mihir Pant, Hari Krovi, Don Towsley, Leandros Tassiulas, Liang Jiang, Prithwish Basu, Dirk Englund, and Saikat Guha. Routing entanglement in the quantum internet. *npj Quantum Information*, 5(1), March 2019. doi: 10.1038/s41534-019-0139-x. URL https://doi.org/10.1038/s41534-019-0139-x.

[42] Daniel Gottesman, Thomas Jennewein, and Sarah Croke. Longer-baseline telescopes using quantum repeaters. *Physical Review Letters*, 109(7), August 2012. doi: 10.1103/physrevlett.109.070503. URL https://doi.org/10.1103/physrevlett.109.070503.

[43] P. Kómár, E. M. Kessler, M. Bishof, L. Jiang, A. S. Sørensen, J. Ye, and M. D. Lukin. A quantum network of clocks. *Nature Physics*, 10(8):582–587, June 2014. doi: 10.1038/nphys3000. URL https://doi.org/10.1038/nphys3000.

[44] Christoph Simon. Towards a global quantum network. *Nature Photonics*, 11(11):678–680, October 2017. doi: 10.1038/s41566-017-0032-0. URL https://doi.org/10.1038/s41566-017-0032-0.

[45] L.-M. Duan, M. D. Lukin, J. I. Cirac, and P. Zoller. Long-distance quantum communication with atomic ensembles and linear optics. *Nature*, 414(6862):413–418, November 2001. doi: 10.1038/35106500. URL https://doi.org/10.1038/35106500.

[46] Nicolas Sangouard, Christoph Simon, Jiří Minář, Hugo Zbinden, Hugues de Riedmatten, and Nicolas Gisin. Long-distance entanglement distribution with single-photon sources. *Physical Review A*, 76(5), November 2007. doi: 10.1103/physreva.76.050301. URL https://doi.org/10.1103/physreva.76.050301.

[47] Maximilian Ruf, Noel H. Wan, Hyeongrak Choi, Dirk Englund, and Ronald Hanson. Quantum networks based on color centers in diamond. *Journal of Applied Physics*, 130(7):070901, August 2021. doi: 10.1063/5.0056534. URL https://doi.org/10.1063/5.0056534.

[48] L.-M. Duan and C. Monroe. Colloquium: Quantum networks with trapped ions. *Rev. Mod. Phys.*, 82:1209–1224, Apr 2010. doi: 10.1103/RevModPhys.82.1209. URL https://link.aps.org/doi/10.1103/RevModPhys.82.1209.

[49] Stephan Ritter, Christian Nölleke, Carolin Hahn, Andreas Reiserer, Andreas Neuzner, Manuel Uphoff, Martin Mücke, Eden Figueroa, Joerg Bochmann, and Gerhard Rempe. An elementary quantum network of single atoms in optical cavities. *Nature*, 484(7393):195–200, April 2012. doi: 10.1038/nature11023. URL https://doi.org/10.1038/nature11023.

[50] Mohammad Mirhosseini, Alp Sipahigil, Mahmoud Kalaee, and Oskar Painter. Superconducting qubit to optical photon transduction. *Nature*, 588(7839):599–603, December 2020. doi: 10.1038/s41586-020-3038-6. URL https://doi.org/10.1038/s41586-020-3038-6.

[51] Stefania Castelletto, Faraz A Inam, Shin ichiro Sato, and Alberto Boretti. Hexagonal boron nitride: a review of the emerging material platform for single-photon sources and the spin–photon interface. *Beilstein Journal of Nanotechnology*, 11:740–769, May 2020. doi: 10.3762/bjnano.11.61. URL https://doi.org/10.3762/bjnano.11.61.

[52] Igor Aharonovich, Dirk Englund, and Milos Toth. Solid-state single-photon emitters. *Nature Photonics*, 10(10):631–641, September 2016. doi: 10.1038/nphoton.2016.186. URL https://doi.org/10.1038/nphoton.2016.186.

[53] Mete Atatüre, Dirk Englund, Nick Vamivakas, Sang-Yun Lee, and Joerg Wrachtrup. Material platforms for spin-based photonic quantum technologies. *Nature Reviews Materials*, 3(5):38–51, April 2018. doi: 10.1038/s41578-018-0008-9. URL https://doi.org/10.1038/s41578-018-0008-9.

[54] Victor Acosta and Philip Hemmer. Nitrogen-vacancy centers: Physics and applications. *MRS Bulletin*, 38(2):127–130, February 2013. doi: 10.1557/mrs.2013.18. URL https://doi.org/10.1557/mrs.2013.18.

[55] P. C. Maurer, G. Kucsko, C. Latta, L. Jiang, N. Y. Yao, S. D. Bennett, F. Pastawski, D. Hunger, N. Chisholm, M. Markham, D. J. Twitchen, J. I. Cirac, and M. D. Lukin. Room-temperature quantum bit memory exceeding one second. *Science*, 336(6086):1283–1286, June 2012. doi: 10.1126/science.1220513. URL https://doi.org/10.1126/science.1220513.

[56] M. Pompili, S. L. N. Hermans, S. Baier, H. K. C. Beukers, P. C. Humphreys, R. N. Schouten, R. F. L. Vermeulen, M. J. Tiggelman, L. dos Santos Martins, B. Dirkse, S. Wehner, and R. Hanson. Realization of a multinode quantum network of remote solid-state qubits. *Science*, 372(6539):259–264, April 2021. doi: 10.1126/science.abg1919. URL https://doi.org/10.1126/science.abg1919.

[57] B. Hensen, H. Bernien, A. E. Dréau, A. Reiserer, N. Kalb, M. S. Blok, J. Ruitenberg, R. F. L. Vermeulen, R. N. Schouten, C. Abellán, W. Amaya, V. Pruneri, M. W. Mitchell, M. Markham, D. J. Twitchen, D. Elkouss, S. Wehner, T. H. Taminiau, and R. Hanson. Loophole-free bell inequality violation using electron spins separated by 1.3 kilometres. *Nature*, 526(7575):682–686, October 2015. doi: 10.1038/nature15759. URL https://doi.org/10.1038/nature15759.

[58] M. H. Abobeih, J. Cramer, M. A. Bakker, N. Kalb, M. Markham, D. J. Twitchen, and T. H. Taminiau. One-second coherence for a single electron spin coupled to a multi-qubit nuclear-spin environment. *Nature Communications*, 9(1), June 2018. doi: 10.1038/s41467-018-04916-z. URL https://doi.org/10.1038/s41467-018-04916-z.

[59] J. Cramer, N. Kalb, M. A. Rol, B. Hensen, M. S. Blok, M. Markham, D. J. Twitchen, R. Hanson, and T. H. Taminiau. Repeated quantum error correction on a continuously encoded qubit by real-time feedback. *Nature Communications*, 7(1), May 2016. doi: 10.1038/ncomms11526. URL https://doi.org/10.1038/ncomms11526.

[60] J. R. Weber, W. F. Koehl, J. B. Varley, A. Janotti, B. B. Buckley, C. G. Van de Walle, and D. D. Awschalom. Quantum computing with defects. *Proceedings of the National Academy of Sciences*, 107 (19):8513–8518, April 2010. doi: 10.1073/pnas.1003052107. URL https://doi.org/10.1073/pnas.1003052107.

[61] Tina Müller, Christian Hepp, Benjamin Pingault, Elke Neu, Stefan Gsell, Matthias Schreck, Hadwig Sternschulte, Doris Steinmüller-Nethl, Christoph Becher, and Mete Atatüre. Optical signatures of silicon-vacancy spins in diamond. *Nature Communications*, 5(1), February 2014. doi: 10.1038/ncomms4328. URL https://doi.org/10.1038/ncomms4328.

[62] Takayuki Iwasaki, Fumitaka Ishibashi, Yoshiyuki Miyamoto, Yuki Doi, Satoshi Kobayashi, Takehide Miyazaki, Kosuke Tahara, Kay D. Jahnke, Lachlan J. Rogers, Boris Naydenov, Fedor Jelezko, Satoshi Yamasaki, Shinji Nagamachi, Toshiro Inubushi, Norikazu Mizuochi, and Mutsuko Hatano. Germanium-vacancy single color centers in diamond. *Scientific Reports*, 5(1), August 2015. doi: 10.1038/srep12882. URL https://doi.org/10.1038/srep12882.

[63] Marina Radulaski, Matthias Widmann, Matthias Niethammer, Jingyuan Linda Zhang, Sang-Yun Lee, Torsten Rendler, Konstantinos G. Lagoudakis, Nguyen Tien Son, Erik Janzén, Takeshi Ohshima, Jörg Wrachtrup, and Jelena Vučković. Scalable quantum photonics with single color centers in silicon carbide. *Nano Letters*, 17(3):1782–1786, February 2017. doi: 10.1021/acs.nanolett.6b05102. URL https://doi.org/10.1021/acs.nanolett.6b05102.

[64] Steffen Michaelis de Vasconcellos, Daniel Wigger, Ursula Wurstbauer, Alexander W. Holleitner, Rudolf Bratschitsch, and Tilmann Kuhn. Single-photon emitters in layered van der waals materials. *physica status solidi (b)*, 259(4):2100566, February 2022. doi: 10.1002/pssb.202100566. URL https://doi.org/10.1002/pssb.202100566.

[65] Chitraleema Chakraborty, Laura Kinnischtzke, Kenneth M. Goodfellow, Ryan Beams, and A. Nick Vamivakas. Voltage-controlled quantum light from an atomically thin semiconductor. *Nature Nanotechnology*, 10(6):507–511, May 2015. doi: 10.1038/nnano.2015.79. URL https://doi.org/10.1038/nnano.2015.79.

[66] Yu-Ming He, Genevieve Clark, John R. Schaibley, Yu He, Ming-Cheng Chen, Yu-Jia Wei, Xing Ding, Qiang Zhang, Wang Yao, Xiaodong Xu, Chao-Yang Lu, and Jian-Wei Pan. Single quantum emitters in monolayer semiconductors. *Nature Nanotechnology*, 10(6):497–502, May 2015. doi: 10.1038/nnano.2015.75. URL https://doi.org/10.1038/nnano.2015.75.

[67] Philipp Tonndorf, Robert Schmidt, Robert Schneider, Johannes Kern, Michele Buscema, Gary A. Steele, Andres Castellanos-Gomez, Herre S. J. van der Zant, Steffen Michaelis de Vasconcellos, and Rudolf Bratschitsch. Single-photon emission from localized excitons in an atomically thin semiconductor. *Optica*, 2(4):347, April 2015. doi: 10.1364/optica.2.000347. URL https://doi.org/10.1364/optica.2.000347.

[68] Toan Trong Tran, Kerem Bray, Michael J. Ford, Milos Toth, and Igor Aharonovich. Quantum emission from hexagonal boron nitride monolayers. *Nature Nanotechnology*, 11(1):37–41, October 2015. doi: 10.1038/nnano.2015.242. URL https://doi.org/10.1038/nnano.2015.242.

[69] Fengnian Xia, Han Wang, Di Xiao, Madan Dubey, and Ashwin Ramasubramaniam. Two-dimensional material nanophotonics. *Nature Photonics*, 8(12):899–907, November 2014. doi: 10.1038/nphoton.2014.271. URL https://doi.org/10.1038/nphoton.2014.271.

[70] G. Cassabois, P. Valvin, and B. Gil. Hexagonal boron nitride is an indirect bandgap semiconductor.

Nature Photonics, 10(4):262–266, January 2016. doi: 10.1038/nphoton.2015.277. URL https://doi.org/10.1038/nphoton.2015.277.

[71] C. Elias, P. Valvin, T. Pelini, A. Summerfield, C. J. Mellor, T. S. Cheng, L. Eaves, C. T. Foxon, P. H. Beton, S. V. Novikov, B. Gil, and G. Cassabois. Direct band-gap crossover in epitaxial monolayer boron nitride. *Nature Communications*, 10(1), June 2019. doi: 10.1038/s41467-019-10610-5. URL https://doi.org/10.1038/s41467-019-10610-5.

[72] Nicholas R. Jungwirth, Brian Calderon, Yanxin Ji, Michael G. Spencer, Michael E. Flatté, and Gregory D. Fuchs. Temperature dependence of wavelength selectable zero-phonon emission from single defects in hexagonal boron nitride. *Nano Letters*, 16(10):6052–6057, September 2016. doi: 10.1021/acs.nanolett.6b01987. URL https://doi.org/10.1021/acs.nanolett.6b01987.

[73] Annemarie L. Exarhos, David A. Hopper, Raj N. Patel, Marcus W. Doherty, and Lee C. Bassett. Magnetic-field-dependent quantum emission in hexagonal boron nitride at room temperature. *Nature Communications*, 10(1), January 2019. doi: 10.1038/s41467-018-08185-8. URL https://doi.org/10.1038/s41467-018-08185-8.

[74] Nicholas V. Proscia, Zav Shotan, Harishankar Jayakumar, Prithvi Reddy, Charles Cohen, Michael Dollar, Audrius Alkauskas, Marcus Doherty, Carlos A. Meriles, and Vinod M. Menon. Near-deterministic activation of room-temperature quantum emitters in hexagonal boron nitride. *Optica*, 5(9):1128, September 2018. doi: 10.1364/optica.5.001128. URL https://doi.org/10.1364/optica.5.001128.

[75] Kumarasiri Konthasinghe, Chitraleema Chakraborty, Nikhil Mathur, Liangyu Qiu, Arunabh Mukherjee, Gregory D. Fuchs, and A. Nick Vamivakas. Rabi oscillations and resonance fluorescence from a single hexagonal boron nitride quantum emitter. *Optica*, 6(5):542, April 2019. doi: 10.1364/optica.6.000542. URL https://doi.org/10.1364/optica.6.000542.

[76] Toan Trong Tran, Christopher Elbadawi, Daniel Totonjian, Charlene J. Lobo, Gabriele Grosso, Hyowon Moon, Dirk R. Englund, Michael J. Ford, Igor Aharonovich, and Milos Toth. Robust multicolor single photon emission from point defects in hexagonal boron nitride. *ACS Nano*, 10(8):7331–7338, July 2016. doi: 10.1021/acsnano.6b03602. URL https://doi.org/10.1021/acsnano.6b03602.

[77] Gabriele Grosso, Hyowon Moon, Benjamin Lienhard, Sajid Ali, Dmitri K. Efetov, Marco M. Furchi, Pablo Jarillo-Herrero, Michael J. Ford, Igor Aharonovich, and Dirk Englund. Tunable and high-purity room temperature single-photon emission from atomic defects in hexagonal boron nitride. *Nature*

Communications, 8(1), September 2017. doi: 10.1038/s41467-017-00810-2. URL https://doi.org/10.1038/s41467-017-00810-2.

[78] Antoine Reserbat-Plantey, Itai Epstein, Iacopo Torre, Antonio T. Costa, P. A. D. Gonçalves, N. Asger Mortensen, Marco Polini, Justin C. W. Song, Nuno M. R. Peres, and Frank H. L. Koppens. Quantum nanophotonics in two-dimensional materials. *ACS Photonics*, 8(1):85–101, January 2021. doi: 10.1021/acsphotonics.0c01224. URL https://doi.org/10.1021/acsphotonics.0c01224.

[79] A. Dietrich, M. W. Doherty, I. Aharonovich, and A. Kubanek. Solid-state single photon source with fourier transform limited lines at room temperature. *Phys. Rev. B*, 101:081401(R), Feb 2020. doi: 10.1103/PhysRevB.101.081401. URL https://link.aps.org/doi/10.1103/PhysRevB.101.081401.

[80] Noah Mendelson, Dipankar Chugh, Jeffrey R. Reimers, Tin S. Cheng, Andreas Gottscholl, Hu Long, Christopher J. Mellor, Alex Zettl, Vladimir Dyakonov, Peter H. Beton, Sergei V. Novikov, Chennupati Jagadish, Hark Hoe Tan, Michael J. Ford, Milos Toth, Carlo Bradac, and Igor Aharonovich. Identifying carbon as the source of visible single-photon emission from hexagonal boron nitride. *Nature Materials*, 20(3):321–328, November 2020. doi: 10.1038/s41563-020-00850-y. URL https://doi.org/10.1038/s41563-020-00850-y.

[81] Mehdi Abdi, Jyh-Pin Chou, Adam Gali, and Martin B. Plenio. Color centers in hexagonal boron nitride monolayers: A group theory and ab initio analysis. *ACS Photonics*, 5(5):1967–1976, April 2018. doi: 10.1021/acsphotonics.7b01442. URL https://doi.org/10.1021/acsphotonics.7b01442.

[82] J R Maze, A Gali, E Togan, Y Chu, A Trifonov, E Kaxiras, and M D Lukin. Properties of nitrogen-vacancy centers in diamond: the group theoretic approach. *New Journal of Physics*, 13(2):025025, February 2011. doi: 10.1088/1367-2630/13/2/025025. URL https://doi.org/10.1088/1367-2630/13/2/025025.

[83] M. W. Doherty, F. Dolde, H. Fedder, F. Jelezko, J. Wrachtrup, N. B. Manson, and L. C. L. Hollenberg. Theory of the ground-state spin of the NV^- center in diamond. *Phys. Rev. B*, 85:205203, May 2012. doi: 10.1103/PhysRevB.85.205203. URL https://link.aps.org/doi/10.1103/PhysRevB.85.205203.

[84] Adam Gali and Jeronimo R. Maze. Ab initio study of the split silicon-vacancy defect in diamond: Electronic structure and related properties. *Phys. Rev. B*, 88:235205, Dec 2013. doi: 10.1103/PhysRevB.88.235205. URL https://link.aps.org/doi/10.1103/PhysRevB.88.235205.

[85] Lachlan J. Rogers, Kay D. Jahnke, Marcus W. Doherty, Andreas Dietrich, Liam P. McGuinness, Christoph Müller, Tokuyuki Teraji, Hitoshi Sumiya, Junichi Isoya, Neil B. Manson, and Fedor Jelezko.

Electronic structure of the negatively charged silicon-vacancy center in diamond. *Physical Review B*, 89(23), June 2014. doi: 10.1103/physrevb.89.235101. URL https://doi.org/10.1103/physrevb.89.235101.

[86] Christoph Freysoldt, Blazej Grabowski, Tilmann Hickel, Jörg Neugebauer, Georg Kresse, Anderson Janotti, and Chris G. Van de Walle. First-principles calculations for point defects in solids. *Reviews of Modern Physics*, 86(1):253–305, March 2014. doi: 10.1103/revmodphys.86.253. URL https://doi.org/10.1103/revmodphys.86.253.

[87] Cesar Jara, Tomáš Rauch, Silvana Botti, Miguel A. L. Marques, Ariel Norambuena, Raul Coto, J. E. Castellanos-Águila, Jeronimo R. Maze, and Francisco Munoz. First-principles identification of single photon emitters based on carbon clusters in hexagonal boron nitride. *The Journal of Physical Chemistry A*, 125(6):1325–1335, February 2021. doi: 10.1021/acs.jpca.0c07339. URL https://doi.org/10.1021/acs.jpca.0c07339.

[88] Michael Hoese, Prithvi Reddy, Andreas Dietrich, Michael K. Koch, Konstantin G. Fehler, Marcus W. Doherty, and Alexander Kubanek. Mechanical decoupling of quantum emitters in hexagonal boron nitride from low-energy phonon modes. *Science Advances*, 6(40), October 2020. doi: 10.1126/sciadv.aba6038. URL https://doi.org/10.1126/sciadv.aba6038.

[89] Philipp Auburger and Adam Gali. Towards ab initio identification of paramagnetic substitutional carbon defects in hexagonal boron nitride acting as quantum bits. *Phys. Rev. B*, 104:075410, Aug 2021. doi: 10.1103/PhysRevB.104.075410. URL https://link.aps.org/doi/10.1103/PhysRevB.104.075410.

[90] Christian Hepp, Tina Müller, Victor Waselowski, Jonas N. Becker, Benjamin Pingault, Hadwig Sternschulte, Doris Steinmüller-Nethl, Adam Gali, Jeronimo R. Maze, Mete Atatüre, and Christoph Becher. Electronic structure of the silicon vacancy color center in diamond. *Phys. Rev. Lett.*, 112: 036405, Jan 2014. doi: 10.1103/PhysRevLett.112.036405. URL https://link.aps.org/doi/10.1103/PhysRevLett.112.036405.

[91] A. Sajid, Jeffrey R. Reimers, and Michael J. Ford. Defect states in hexagonal boron nitride: Assignments of observed properties and prediction of properties relevant to quantum computation. *Phys. Rev. B*, 97:064101, Feb 2018. doi: 10.1103/PhysRevB.97.064101. URL https://link.aps.org/doi/10.1103/PhysRevB.97.064101.

[92] Daniel Manzano. A short introduction to the lindblad master equation. *AIP Advances*, 10(2):025106, February 2020. doi: 10.1063/1.5115323. URL https://doi.org/10.1063/1.5115323.

[93] Michael Tinkham. *Group theory and quantum mechanics*. Dover Publications, Inc, Mineola, New York, 2003. ISBN 9780486432472. URL https://books.google.ca/books?id=xdwoAwAAQBAJ.

[94] J.F. Cornwell. *Group Theory in Physics: An Introduction*. Number v. 1 in Group Theory in Physics. Academic Press, San Diego, California, 1997. doi: 10.1016/B978-0-12-189800-7.X5000-6. URL https://doi.org/10.1016/B978-0-12-189800-7.X5000-6.

[95] Willard Miller. *Symmetry groups and their applications*. Pure and applied mathematics; a series of monographs and textbooks. Academic Press, New York, 1972. ISBN 9780124974609.

[96] B. D. Sharma. Crystallographic and spectroscopic symmetry notations. *Journal of Chemical Education*, 59(7):554, July 1982. doi: 10.1021/ed059p554. URL https://doi.org/10.1021/ed059p554.

[97] John Preskill. Lecture notes for physics 219/computer science 219: Quantum computation, 2020. URL http://theory.caltech.edu/~preskill/ph219/index.html.

[98] Paola Cappellaro. Lecture notes for 22.51 quantum theory of radiation interactions, 2012. URL https://ocw.mit.edu/courses/22-51-quantum-theory-of-radiation-interactions-fall-2012/pages/lecture-notes/.

[99] B. Kraus, H. P. Büchler, S. Diehl, A. Kantian, A. Micheli, and P. Zoller. Preparation of entangled states by quantum markov processes. *Physical Review A*, 78(4), October 2008. doi: 10.1103/physreva.78.042307. URL https://doi.org/10.1103/physreva.78.042307.

[100] G. Lindblad. On the generators of quantum dynamical semigroups. *Communications in Mathematical Physics*, 48(2):119–130, June 1976. doi: 10.1007/bf01608499. URL https://doi.org/10.1007/bf01608499.

[101] Vittorio Gorini. Completely positive dynamical semigroups of n-level systems. *Journal of Mathematical Physics*, 17(5):821, 1976. doi: 10.1063/1.522979. URL https://doi.org/10.1063/1.522979.

[102] Victor V. Albert. Lindbladians with multiple steady states: theory and applications. 2018. doi: 10.48550/ARXIV.1802.00010. URL https://arxiv.org/abs/1802.00010.

[103] Howard J. Carmichael. *Statistical Methods in Quantum Optics 1*. Springer Berlin Heidelberg, Berlin, Heidelberg, 1999. ISBN 9783642081330. doi: 10.1007/978-3-662-03875-8. URL http://link.springer.com/10.1007/978-3-662-03875-8.

[104] Ángel Rivas, A Douglas K Plato, Susana F Huelga, and Martin B Plenio. Markovian master equations: a critical study. *New Journal of Physics*, 12(11):113032, nov 2010. doi: 10.1088/1367-2630/12/11/113032. URL https://doi.org/10.1088/1367-2630/12/11/113032.

[105] Donatella Carbonera. Optically detected magnetic resonance (ODMR) of photoexcited triplet states. *Photosynthesis Research*, 102(2-3):403–414, February 2009. doi: 10.1007/s11120-009-9407-5. URL https://doi.org/10.1007/s11120-009-9407-5.

[106] J. Schmidt and J.H. Van Der Waals. Optical detection of zero-field transitions in phosphorescent triplet states. *Chemical Physics Letters*, 2(8):640–642, December 1968. doi: 10.1016/0009-2614(63)80039-1. URL https://doi.org/10.1016/0009-2614(63)80039-1.

[107] A. Gruber, A. Dräbenstedt, C. Tietz, L. Fleury, J. Wrachtrup, and C. von Borczyskowski. Scanning confocal optical microscopy and magnetic resonance on single defect centers. *Science*, 276(5321):2012–2014, June 1997. doi: 10.1126/science.276.5321.2012. URL https://doi.org/10.1126/science.276.5321.2012.

[108] Lilian Childress and Ronald Hanson. Diamond NV centers for quantum computing and quantum networks. *MRS Bulletin*, 38(2):134–138, February 2013. doi: 10.1557/mrs.2013.20. URL https://doi.org/10.1557/mrs.2013.20.

[109] Marcus W. Doherty, Neil B. Manson, Paul Delaney, Fedor Jelezko, Jörg Wrachtrup, and Lloyd C.L. Hollenberg. The nitrogen-vacancy colour centre in diamond. *Physics Reports*, 528(1):1–45, July 2013. doi: 10.1016/j.physrep.2013.02.001. URL https://doi.org/10.1016/j.physrep.2013.02.001.

[110] Pauli Kehayias. Exploring basic properties and applications of nitrogen-vacancy color centers in diamond, May 2018. URL https://thesiscommons.org/db5fy.

[111] Andreas Gottscholl, Mehran Kianinia, Victor Soltamov, Sergei Orlinskii, Georgy Mamin, Carlo Bradac, Christian Kasper, Klaus Krambrock, Andreas Sperlich, Milos Toth, Igor Aharonovich, and Vladimir Dyakonov. Initialization and read-out of intrinsic spin defects in a van der waals crystal at room temperature. *Nature Materials*, 19(5):540–545, February 2020. doi: 10.1038/s41563-020-0619-6. URL https://doi.org/10.1038/s41563-020-0619-6.

[112] Nathan Chejanovsky, Amlan Mukherjee, Jianpei Geng, Yu-Chen Chen, Youngwook Kim, Andrej Denisenko, Amit Finkler, Takashi Taniguchi, Kenji Watanabe, Durga Bhaktavatsala Rao Dasari, Philipp Auburger, Adam Gali, Jurgen H. Smet, and Jörg Wrachtrup. Single-spin resonance in a

van der waals embedded paramagnetic defect. *Nature Materials*, 20(8):1079–1084, May 2021. doi: 10.1038/s41563-021-00979-4. URL https://doi.org/10.1038/s41563-021-00979-4.

[113] Gichang Noh, Daebok Choi, Jin-Hun Kim, Dong-Gil Im, Yoon-Ho Kim, Hosung Seo, and Jieun Lee. Stark tuning of single-photon emitters in hexagonal boron nitride. *Nano Letters*, 18(8):4710–4715, June 2018. doi: 10.1021/acs.nanolett.8b01030. URL https://doi.org/10.1021/acs.nanolett.8b01030.

[114] K. B. Lipkowitz and D. B. Boyd, editors. *Reviews in Computational Chemistry*, volume 17. Wiley-VCH, New York, 2001.

[115] A M Stoneham. Non-radiative transitions in semiconductors. *Reports on Progress in Physics*, 44 (12):1251–1295, dec 1981. doi: 10.1088/0034-4885/44/12/001. URL https://doi.org/10.1088/0034-4885/44/12/001.

[116] M. L. Goldman, M. W. Doherty, A. Sipahigil, N. Y. Yao, S. D. Bennett, N. B. Manson, A. Kubanek, and M. D. Lukin. State-selective intersystem crossing in nitrogen-vacancy centers. *Phys. Rev. B*, 91: 165201, Apr 2015. doi: 10.1103/PhysRevB.91.165201. URL https://link.aps.org/doi/10.1103/PhysRevB.91.165201.

[117] M. L. Goldman, A. Sipahigil, M. W. Doherty, N. Y. Yao, S. D. Bennett, M. Markham, D. J. Twitchen, N. B. Manson, A. Kubanek, and M. D. Lukin. Phonon-induced population dynamics and intersystem crossing in nitrogen-vacancy centers. *Phys. Rev. Lett.*, 114:145502, Apr 2015. doi: 10.1103/PhysRevLett.114.145502. URL https://link.aps.org/doi/10.1103/PhysRevLett.114.145502.

[118] C. Simon, M. Afzelius, J. Appel, A. Boyer de la Giroday, S. J. Dewhurst, N. Gisin, C. Y. Hu, F. Jelezko, S. Kröll, J. H. Müller, J. Nunn, E. S. Polzik, J. G. Rarity, H. De Riedmatten, W. Rosenfeld, A. J. Shields, N. Sköld, R. M. Stevenson, R. Thew, I. A. Walmsley, M. C. Weber, H. Weinfurter, J. Wrachtrup, and R. J. Young. Quantum memories. *The European Physical Journal D*, 58(1):1–22, April 2010. doi: 10.1140/epjd/e2010-00103-y. URL https://doi.org/10.1140/epjd/e2010-00103-y.

[119] G. D. Fuchs, G. Burkard, P. V. Klimov, and D. D. Awschalom. A quantum memory intrinsic to single nitrogen–vacancy centres in diamond. *Nature Physics*, 7(10):789–793, June 2011. doi: 10.1038/nphys2026. URL https://doi.org/10.1038/nphys2026.

[120] J. H. Shim, I. Niemeyer, J. Zhang, and D. Suter. Room-temperature high-speed nuclear-spin quantum memory in diamond. *Phys. Rev. A*, 87:012301, Jan 2013. doi: 10.1103/PhysRevA.87.012301. URL https://link.aps.org/doi/10.1103/PhysRevA.87.012301.

[121] Marcis Auzinsh, Andris Berzins, Dmitry Budker, Laima Busaite, Ruvin Ferber, Florian Gahbauer, Reinis Lazda, Arne Wickenbrock, and Huijie Zheng. Hyperfine level structure in nitrogen-vacancy centers near the ground-state level anticrossing. *Phys. Rev. B*, 100:075204, Aug 2019. doi: 10.1103/PhysRevB.100.075204. URL https://link.aps.org/doi/10.1103/PhysRevB.100.075204.

[122] Arthur Marshall Stoneham. *Theory of defects in solids: electronic structure of defects in insulators and semiconductors*. Clarendon Press; Oxford University Press, Oxford, New York, 2001. ISBN 9780198507802.

[123] M. Mackoit-Sinkevičienė, M. Maciaszek, C. G. Van de Walle, and A. Alkauskas. Carbon dimer defect as a source of the 4.1 eV luminescence in hexagonal boron nitride. *Applied Physics Letters*, 115(21): 212101, November 2019. doi: 10.1063/1.5124153. URL https://doi.org/10.1063/1.5124153.

[124] Ádám Gali. Ab initio theory of the nitrogen-vacancy center in diamond. *Nanophotonics*, 8(11): 1907–1943, September 2019. doi: 10.1515/nanoph-2019-0154. URL https://doi.org/10.1515/nanoph-2019-0154.

[125] Seong-Yeon Lee, Tae-Young Jeong, Suyong Jung, and Ki-Ju Yee. Refractive index dispersion of hexagonal boron nitride in the visible and near-infrared. *physica status solidi (b)*, 256(6):1800417, October 2018. doi: 10.1002/pssb.201800417. URL https://doi.org/10.1002/pssb.201800417.

[126] Audrius Alkauskas, Qimin Yan, and Chris G Van de Walle. First-principles theory of nonradiative carrier capture via multiphonon emission. *Physical Review B*, 90(7):075202, 2014. URL https://journals.aps.org/prb/abstract/10.1103/PhysRevB.90.075202.

[127] Feng Wu, Tyler J. Smart, Junqing Xu, and Yuan Ping. Carrier recombination mechanism at defects in wide band gap two-dimensional materials from first principles. *Phys. Rev. B*, 100:081407(R), Aug 2019. doi: 10.1103/PhysRevB.100.081407. URL https://link.aps.org/doi/10.1103/PhysRevB.100.081407.

[128] Mark E Turiansky, Audrius Alkauskas, Manuel Engel, Georg Kresse, Darshana Wickramaratne, Jimmy-Xuan Shen, Cyrus E Dreyer, and Chris G Van de Walle. Nonrad: Computing nonradiative capture coefficients from first principles. *Computer Physics Communications*, page 108056, 2021. URL https://www.sciencedirect.com/science/article/pii/S0010465521001685.

[129] Tyler J. Smart, Kejun Li, Junqing Xu, and Yuan Ping. Intersystem crossing and exciton–defect coupling of spin defects in hexagonal boron nitride. *npj Computational Materials*, 7(1):59, Dec

2021. ISSN 2057-3960. doi: 10.1038/s41524-021-00525-5. URL http://www.nature.com/articles/s41524-021-00525-5.

[130] T. Nakamura, M. Wada, K. Okada, A. Takamine, Y. Ishida, Y. Yamazaki, T. Kambara, Y. Kanai, T. M. Kojima, Y. Nakai, N. Oshima, A. Yoshida, T. Kubo, S. Ohtani, K. Noda, I. Katayama, V. Lioubimov, H. Wollnik, V. Varentsov, and H. A. Schuessler. Laser spectroscopy of $^{7,10}Be^{+}$ in an online ion trap. *Phys. Rev. A*, 74:052503, Nov 2006. doi: 10.1103/PhysRevA.74.052503. URL https://link.aps.org/doi/10.1103/PhysRevA.74.052503.

[131] D. H. Slichter, V. B. Verma, D. Leibfried, R. P. Mirin, S. W. Nam, and D. J. Wineland. UV-sensitive superconducting nanowire single photon detectors for integration in an ion trap. *Optics Express*, 25 (8):8705, April 2017. doi: 10.1364/oe.25.008705. URL https://doi.org/10.1364/oe.25.008705.

[132] G. Clos, M. Enderlein, U. Warring, T. Schaetz, and D. Leibfried. Decoherence-assisted spectroscopy of a single mg^{+} ion. *Phys. Rev. Lett.*, 112:113003, Mar 2014. doi: 10.1103/PhysRevLett.112.113003. URL https://link.aps.org/doi/10.1103/PhysRevLett.112.113003.

[133] Mads K. Boll, Ilya P. Radko, Alexander Huck, and Ulrik L. Andersen. Photophysics of quantum emitters in hexagonal boron-nitride nano-flakes. *Optics Express*, 28(5):7475, February 2020. doi: 10.1364/oe.386629. URL https://doi.org/10.1364/oe.386629.

[134] Andreas Gottscholl, Matthias Diez, Victor Soltamov, Christian Kasper, Andreas Sperlich, Mehran Kianinia, Carlo Bradac, Igor Aharonovich, and Vladimir Dyakonov. Room temperature coherent control of spin defects in hexagonal boron nitride. *Science Advances*, 7(14), April 2021. doi: 10.1126/sciadv.abf3630. URL https://doi.org/10.1126/sciadv.abf3630.

[135] Paolo Giannozzi, Stefano Baroni, Nicola Bonini, Matteo Calandra, Roberto Car, Carlo Cavazzoni, Davide Ceresoli, Guido L Chiarotti, Matteo Cococcioni, Ismaila Dabo, et al. Quantum espresso: a modular and open-source software project for quantum simulations of materials. *Journal of Physics: Condensed Matter*, 21(39):395502, 2009. URL https://iopscience.iop.org/article/10.1088/0953-8984/21/39/395502/meta.

[136] P. E. Blöchl. Projector augmented-wave method. *Phys. Rev. B*, 50:17953–17979, Dec 1994. doi: 10.1103/PhysRevB.50.17953. URL https://link.aps.org/doi/10.1103/PhysRevB.50.17953.

[137] John P. Perdew, Kieron Burke, and Matthias Ernzerhof. Generalized gradient approximation made simple. *Phys. Rev. Lett.*, 77:3865–3868, Oct 1996. doi: 10.1103/PhysRevLett.77.3865. URL https://link.aps.org/doi/10.1103/PhysRevLett.77.3865.

[138] F Ferreira, AJ Chaves, NMR Peres, and RM Ribeiro. Excitons in hexagonal boron nitride single-layer: a new platform for polaritonics in the ultraviolet. *JOSA B*, 36(3):674–683, 2019. URL https://www.osapublishing.org/josab/fulltext.cfm?uri=josab-36-3-674&id=405086.

[139] Jochen Heyd, Gustavo E Scuseria, and Matthias Ernzerhof. Hybrid functionals based on a screened coulomb potential. *The Journal of Chemical Physics*, 118(18):8207–8215, 2003. URL https://aip.scitation.org/doi/abs/10.1063/1.1564060.

[140] Darshana Wickramaratne, Leigh Weston, and Chris G. Van de Walle. Monolayer to bulk properties of hexagonal boron nitride. *The Journal of Physical Chemistry C*, 122(44):25524–25529, October 2018. doi: 10.1021/acs.jpcc.8b09087. URL https://doi.org/10.1021/acs.jpcc.8b09087.

[141] Adam Gali, Erik Janzén, Péter Deák, Georg Kresse, and Efthimios Kaxiras. Theory of spin-conserving excitation of the $N - V^-$ center in diamond. *Phys. Rev. Lett.*, 103:186404, Oct 2009. doi: 10.1103/PhysRevLett.103.186404. URL https://link.aps.org/doi/10.1103/PhysRevLett.103.186404.

[142] Jeffrey R Reimers, Ali Sajid, Rika Kobayashi, and Michael J Ford. Understanding and calibrating density-functional-theory calculations describing the energy and spectroscopy of defect sites in hexagonal boron nitride. *Journal of Chemical Theory and Computation*, 14(3):1602–1613, 2018. URL https://pubs.acs.org/doi/abs/10.1021/acs.jctc.7b01072.

[143] Daniel H Ess, Erin R Johnson, Xiangqian Hu, and Weitao Yang. Singlet- triplet energy gaps for diradicals from fractional-spin density-functional theory. *The Journal of Physical Chemistry A*, 115 (1):76–83, 2011. URL https://pubs.acs.org/doi/abs/10.1021/jp109280y.

[144] Kejun Li, Tyler Smart, and Yuan Ping. c_2c_n as a 2 ev single-photon emitter candidate in hexagonal boron nitride. *arXiv preprint arXiv:2110.01787*, 2021. doi: 10.48550/ARXIV.2110.01787. URL https://arxiv.org/abs/2110.01787.

[145] Marek Maciaszek, Lukas Razinkovas, and Audrius Alkauskas. Thermodynamics of carbon point defects in hexagonal boron nitride. *Physical Review Materials*, 6(1), January 2022. doi: 10.1103/physrevmaterials.6.014005. URL https://doi.org/10.1103/physrevmaterials.6.014005.

Appendix A

Matrix elements of the Hamiltonian

In this chapter, we provide the matrix elements of the interactions discussed in the main text.

A.1 Spin-orbit interaction

The matrix elements of the spin-orbit interaction are given below, where the variables λ, and λ' are defined as

$$\lambda = \langle a|l^{(y)}|b\rangle, \lambda' = \langle b'|l^{(y)}|a\rangle. \tag{A.1}$$

$$H_{\rm so} = \frac{i}{2}\times \tag{A.2}$$

	$\mathcal{A}^{0,d}_{+1/2}$	$\mathcal{A}^{0,d}_{-1/2}$	$\mathcal{B}^{1,d}_{+1/2}$	$\mathcal{B}^{1,d}_{-1/2}$	$\mathcal{B}^{2,d}_{+1/2}$	$\mathcal{B}^{2,d}_{-1/2}$	$\mathcal{A}^{3,q}_{+1/2}$	$\mathcal{A}^{3,q}_{-1/2}$	$\mathcal{A}^{3,q}_{+3/2}$	$\mathcal{A}^{3,q}_{-3/2}$	$\mathcal{A}^{3,d'}_{+1/2}$	$\mathcal{A}^{3,d'}_{-1/2}$	$\mathcal{A}^{3,d''}_{+1/2}$	$\mathcal{A}^{3,d''}_{-1/2}$
$\mathcal{A}^{0,d}_{+1/2}$	0													
$\mathcal{A}^{0,d}_{-1/2}$	0	0												
$\mathcal{B}^{1,d}_{+1/2}$	0	$-\lambda$	0											
$\mathcal{B}^{1,d}_{-1/2}$	λ	0	0	0										
$\mathcal{B}^{2,d}_{+1/2}$	0	$-\lambda'$	0	0	0									
$\mathcal{B}^{2,d}_{-1/2}$	λ'	0	0	0	0	0								
$\mathcal{A}^{3,q}_{+1/2}$	0	0	0	$-\frac{\lambda'}{\sqrt{3}}$	0	$-\frac{\lambda}{\sqrt{3}}$	0							
$\mathcal{A}^{3,q}_{-1/2}$	0	0	$-\frac{\lambda'}{\sqrt{3}}$	0	$-\frac{\lambda}{\sqrt{3}}$	0	0	0						
$\mathcal{A}^{3,q}_{+3/2}$	0	0	$-\lambda'$	0	$-\lambda$	0	0	0	0					
$\mathcal{A}^{3,q}_{-3/2}$	0	0	0	$-\lambda'$	0	$-\lambda$	0	0	0	0				
$\mathcal{A}^{3,d'}_{+1/2}$	0	0	0	$-\frac{\lambda'}{2\sqrt{3}}$	0	$\frac{\lambda}{\sqrt{3}}$	0	0	0	0	0			
$\mathcal{A}^{3,d'}_{-1/2}$	0	0	$-\frac{\lambda'}{2\sqrt{3}}$	0	$\frac{\lambda}{\sqrt{3}}$	0	0	0	0	0	0	0		
$\mathcal{A}^{3,d''}_{+1/2}$	0	0	0	$\frac{\lambda'}{2}$	0	0	0	0	0	0	0	0	0	
$\mathcal{A}^{3,d''}_{-1/2}$	0	0	$\frac{\lambda'}{2}$	0	0	0	0	0	0	0	0	0	0	0

A.2 Spin-spin interaction

We can see from Table 5.3 that only elements of D that transform as IRs A_1 and B_1 would yield nonzero values. These are $\hat{D}^{A_1} = \{\hat{D}_{xx}, \hat{D}_{yy}, \hat{D}_{zz}\}$ and $\hat{D}^{B_1} = (\hat{D}_{xz} + \hat{D}_{zx})/2$. In this interaction, we have the product of two rank-two tensors (see Table A.1). This product can be reduced to a sum of rank four, three, two, one, and zero irreducible tensor operators. Nevertheless, here we need a compound tensor operator of rank zero. This tensor product is given by the equation below [114]:

$$[\hat{\boldsymbol{s}}^{(2)} \otimes \hat{D}^{(2)}]^{(0)}_0 = \frac{1}{\sqrt{5}} \sum_{q=-2}^{+2} (-1)^{2-q} \hat{\boldsymbol{s}}^{(2)}_{-q} \hat{\boldsymbol{D}}^{(2)}_q. \tag{A.3}$$

To use Eq. (A.3), we need the spherical components of $\hat{\boldsymbol{D}}$. Spherical and Cartesian components of $\hat{\boldsymbol{D}}$ are related by the equations below.

Compound tensor	q	Spherical component
$\{\hat{s}_i^{(1)} \otimes \hat{s}_j^{(1)}\}_q^{(2)}$	+2	$\hat{s}_{i,+1}^{(1)}\hat{s}_{j,+1}^{(1)}$
	+1	$(\hat{s}_{i,+1}^{(1)}\hat{s}_{j,0}^{(1)} + \hat{s}_{i,0}^{(1)}\hat{s}_{j,+1}^{(1)})/\sqrt{2}$
	0	$\frac{1}{\sqrt{6}}(\hat{s}_{i,-1}^{(1)}\hat{s}_{j,+1}^{(1)} + 2\hat{s}_{i,0}^{(1)}\hat{s}_{j,0}^{(1)} + \hat{s}_{i,+1}^{(1)}\hat{s}_{j,-1}^{(1)})$
	-1	$(\hat{s}_{i,-1}^{(1)}\hat{s}_{j,0}^{(1)} + \hat{s}_{i,0}^{(1)}\hat{s}_{j,-1}^{(1)})/\sqrt{2}$
	-2	$\hat{s}_{i,-1}^{(1)}\hat{s}_{j,-1}^{(1)}$

Table A.1: Second-rank spin tensor.

$$\begin{aligned}
\hat{\boldsymbol{D}}_{\pm 2}^{(2)} &= (\hat{\boldsymbol{D}}_{xx}^{(2)} - \hat{\boldsymbol{D}}_{yy}^{(2)} \pm 2i\hat{\boldsymbol{D}}_{xy}^{(2)})/\sqrt{2} \\
\hat{\boldsymbol{D}}_{\pm 1}^{(2)} &= \mp(\hat{\boldsymbol{D}}_{xz}^{(2)} \pm i\hat{\boldsymbol{D}}_{yz}^{(2)}) \\
\hat{\boldsymbol{D}}_{0}^{(2)} &= (2\hat{\boldsymbol{D}}_{zz}^{(2)} - \hat{\boldsymbol{D}}_{xx}^{(2)} - \hat{\boldsymbol{D}}_{yy}^{(2)})/\sqrt{6}
\end{aligned} \tag{A.4}$$

The components of $\hat{\boldsymbol{s}}^{(1)}$ in the notation of spherical tensor operators are given by

$$\begin{aligned}
\hat{\boldsymbol{s}}_{+1}^{(1)} &= -\frac{1}{\sqrt{2}}(\hat{\boldsymbol{s}}_x + i\hat{\boldsymbol{s}}_y), \\
\hat{\boldsymbol{s}}_{0}^{(1)} &= \hat{\boldsymbol{s}}_z, \\
\hat{\boldsymbol{s}}_{-1}^{(1)} &= \frac{1}{\sqrt{2}}(\hat{\boldsymbol{s}}_x - i\hat{\boldsymbol{s}}_y), \\
\hat{\boldsymbol{s}}_{+1}^{(1)}|-\frac{1}{2}\rangle &= -\frac{1}{\sqrt{2}}|+\frac{1}{2}\rangle, \\
\hat{\boldsymbol{s}}_{-1}^{(1)}|+\frac{1}{2}\rangle &= \frac{1}{\sqrt{2}}|-\frac{1}{2}\rangle.
\end{aligned} \tag{A.5}$$

Now that we have all the preliminary tools, we will derive the matrix elements. For the elements in the form of $\langle\mathcal{A}|H_{\rm ss}|\mathcal{A}'\rangle$ and $\langle\mathcal{B}|H_{\rm ss}|\mathcal{B}'\rangle$, according to Table 5.3, only the parts of $H_{\rm ss}$ that transform as IR A_1 would yield nonzero values. $|\mathcal{A}\rangle$ and $|\mathcal{A}'\rangle$ can be any of states in Table 5.2 that transform as IR A_2 and similarly $|\mathcal{B}\rangle$ and $|\mathcal{B}'\rangle$ can be any of states in Table 5.2 that transform as IR B_2. $\{\hat{\boldsymbol{D}}_{xx}, \hat{\boldsymbol{D}}_{yy}, \hat{\boldsymbol{D}}_{zz}\}$ are the only components of $\hat{\boldsymbol{D}}$ that transform as IR A_1. In the spherical tensor form, $\hat{\boldsymbol{D}}_0$ transforms as IR A_1 and first two components of $\hat{\boldsymbol{D}}_{\pm 2}$ also transform as IR A_1. Therefore, just $\hat{\boldsymbol{D}}_0$, and $\hat{\boldsymbol{D}}_{\pm 2}$ contribute to nonzero values. At last, according to Eq. (A.3), $\Delta S \in \{0, \pm 2\}$. Similarly, for $\langle\mathcal{A}|H_{\rm ss}|\mathcal{B}\rangle$ according to Table 5.3, only the parts of $H_{\rm ss}$ that transform as IR B_1 would yield nonzero values. $\{\hat{\boldsymbol{D}}_{xz}, \hat{\boldsymbol{D}}_{zx}\}$ are the only components of $\hat{\boldsymbol{D}}$ that transform as IR B_1. Therefore, just $\hat{\boldsymbol{D}}_{\pm 1}$ contributes to nonzero values. For these matrix elements, according to Eq. (A.3), we have $\Delta S \in \{\pm 1\}$.

$$\left.\begin{matrix}\langle\mathcal{A}|H_{\rm ss}|\mathcal{A}'\rangle\\ \langle\mathcal{B}|H_{\rm ss}|\mathcal{B}'\rangle\end{matrix}\right\}\rightarrow A_1\rightarrow\hat{\boldsymbol{D}}_0,\ \hat{\boldsymbol{D}}_{\pm2}\rightarrow\Delta S\in\{0,\pm2\}$$
$$\langle\mathcal{A}|H_{\rm ss}|\mathcal{B}\rangle\rightarrow B_1\rightarrow\hat{\boldsymbol{D}}_{\pm1}\rightarrow\Delta S\in\{\pm1\} \tag{A.6}$$

After doing all the calculations, we get the matrix elements for the spin-spin interaction, shown below.

$$H_{\rm ss}=\frac{\mu_0\gamma_{\rm e}^2\hbar^2}{16\pi}\times \tag{A.7}$$

	$\mathcal{A}^{0,d}_{+1/2}$	$\mathcal{A}^{0,d}_{-1/2}$	$\mathcal{B}^{1,d}_{+1/2}$	$\mathcal{B}^{1,d}_{-1/2}$	$\mathcal{B}^{2,d}_{+1/2}$	$\mathcal{B}^{2,d}_{-1/2}$	$\mathcal{A}^{3,q}_{+1/2}$	$\mathcal{A}^{3,q}_{-1/2}$	$\mathcal{A}^{3,q}_{+3/2}$	$\mathcal{A}^{3,q}_{-3/2}$	$\mathcal{A}^{3,d'}_{+1/2}$	$\mathcal{A}^{3,d'}_{-1/2}$	$\mathcal{A}^{3,d''}_{+1/2}$	$\mathcal{A}^{3,d''}_{-1/2}$
$\mathcal{A}^{0,d}_{+1/2}$	0													
$\mathcal{A}^{0,d}_{-1/2}$	0	0												
$\mathcal{B}^{1,d}_{+1/2}$	0	0	0											
$\mathcal{B}^{1,d}_{-1/2}$	0	0	0	0										
$\mathcal{B}^{2,d}_{+1/2}$	0	0	0	0	0									
$\mathcal{B}^{2,d}_{-1/2}$	0	0	0	0	0	0								
$\mathcal{A}^{3,q}_{+1/2}$	$\mathcal{E}_1$	0	0	$-\mathcal{F}_1$	0	$\mathcal{F}_2$	$-\mathcal{D}_0$							
$\mathcal{A}^{3,q}_{-1/2}$	0	$-\mathcal{E}_1$	$\mathcal{F}_1$	0	$-\mathcal{F}_2$	0	0	$-\mathcal{D}_0$						
$\mathcal{A}^{3,q}_{+3/2}$	0	$-\mathcal{E}_2$	$\frac{-1}{\sqrt{3}}\mathcal{F}_1$	0	$\frac{1}{\sqrt{3}}\mathcal{F}_2$	0	0	$\mathcal{E}_3$	$\mathcal{D}_0$					
$\mathcal{A}^{3,q}_{-3/2}$	$\mathcal{E}_2$	0	0	$\frac{1}{\sqrt{3}}\mathcal{F}_1$	0	$\frac{-1}{\sqrt{3}}\mathcal{F}_2$	$\mathcal{E}_3$	0	0	$\mathcal{D}_0$				
$\mathcal{A}^{3,d'}_{+1/2}$	0	0	0	$-\mathcal{G}$	0	0	$-\mathcal{H}$	0	0	$\mathcal{K}^*$	0			
$\mathcal{A}^{3,d'}_{-1/2}$	0	0	$-\mathcal{G}$	0	0	0	0	$-\mathcal{H}$	$\mathcal{K}^*$	0	0	0		
$\mathcal{A}^{3,d''}_{+1/2}$	0	0	0	0	0	0	$\mathcal{I}$	0	0	$\mathcal{L}^*$	$\mathcal{J}$	0	0	
$\mathcal{A}^{3,d''}_{-1/2}$	0	0	0	0	0	0	0	$\mathcal{I}$	$\mathcal{L}^*$	0	0	$\mathcal{J}$	0	0

The matrix elements used above are defined as

$$
\begin{aligned}
\mathcal{D}_0 &= \frac{1}{2\sqrt{5}}\Big(\langle bb'-b'b|\hat{D}^{(2)}_{zz}|bb'-b'b\rangle \\
&\qquad +\langle ba-ab|\hat{D}^{(2)}_{zz}|ba-ab\rangle \\
&\qquad +\langle ab'-b'a|\hat{D}^{(2)}_{zz}|ab'-b'a\rangle\Big), \\
\mathcal{E}_1 &= \frac{1}{15}\langle ab'-b'a|\hat{D}^{(2)}_{zz}|ab-ba\rangle, \\
\mathcal{E}_2 &= \frac{1}{10}\langle ab'-b'a|\hat{D}^{(2)}_{xx}-\hat{D}^{(2)}_{yy}|ab-ba\rangle, \\
\mathcal{E}_3 &= \frac{1}{\sqrt{30}}\Big(\langle ab'-b'a|\hat{D}^{(2)}_{xx}-\hat{D}^{(2)}_{yy}|ab'-b'a\rangle \\
&\qquad +\langle bb'-b'b|\hat{D}^{(2)}_{xx}-\hat{D}^{(2)}_{yy}|bb'-b'b\rangle \\
&\qquad +\langle ab-ba|\hat{D}^{(2)}_{xx}-\hat{D}^{(2)}_{yy}|ab-ba\rangle\Big), \\
\mathcal{F}_1 &= \frac{\sqrt{3}}{2\sqrt{5}}\langle bb'-b'b|\hat{D}^{(2)}_{xz}|ab-ba\rangle, \\
\mathcal{F}_2 &= \frac{\sqrt{3}}{2\sqrt{5}}\langle ab'-b'a|\hat{D}^{(2)}_{xz}|bb'-b'b\rangle,
\end{aligned}
\tag{A.8}
$$

$$
\begin{aligned}
\mathcal{G} &= \frac{1}{\sqrt{30}}\langle bb'-b'b|\hat{D}^{(2)}_{xz}|ba-ab\rangle, \\
\mathcal{H} &= \frac{1}{6\sqrt{10}}\{\langle bb'-b'b|\hat{D}^{(2)}_{zz}|bb'-b'b\rangle \\
&\qquad +\langle ba-ab|\hat{D}^{(2)}_{zz}|ba-ab\rangle \\
&\qquad -2\langle ab'-b'a|\hat{D}^{(2)}_{zz}|ab'-b'a\rangle\}, \\
\mathcal{I} &= \frac{\sqrt{3}}{2\sqrt{10}}\{-\langle bb'-b'b|\hat{D}^{(2)}_{zz}|bb'-b'b\rangle \\
&\qquad +\langle ab'-b'a|\hat{D}^{(2)}_{zz}|ab'-b'a\rangle\}, \\
\mathcal{J} &= -\frac{1}{2\sqrt{15}}\langle ab'-b'a|\hat{D}^{(2)}_{zz}|ab'-b'a\rangle, \\
\mathcal{K} &= \frac{1}{2\sqrt{15}}\{+\langle ab'-b'a|(\hat{D}^{(2)}_{xx}-\hat{D}^{(2)}_{yy})|ab'-b'a\rangle \\
&\qquad +\langle bb'-b'b|(\hat{D}^{(2)}_{xx}-\hat{D}^{(2)}_{yy})|bb'-b'b\rangle \\
&\qquad -2\langle ba-ab|(\hat{D}^{(2)}_{xx}-\hat{D}^{(2)}_{yy})|ba-ab\rangle\}, \\
\mathcal{L} &= \frac{1}{2\sqrt{5}}\{-\langle ab'-b'a|(\hat{D}^{(2)}_{xx}-\hat{D}^{(2)}_{yy})|ab'-b'a\rangle \\
&\qquad +\langle bb'-b'b|(\hat{D}^{(2)}_{xx}-\hat{D}^{(2)}_{yy})|bb'-b'b\rangle\}.
\end{aligned}
\tag{A.9}
$$

A.3 Dipole transitions

The dipole allowed transition rates would be proportional to the values defined below.

$$
\begin{aligned}
\mu_x &= eE_x\langle a|x|b\rangle \qquad \text{(A.10)}\\
\mu'_x &= eE_x\langle a|x|b'\rangle \\
\mu_{z,0} &= eE_z\{\langle b|z|b\rangle + \langle a|z|a\rangle + \langle b'|z|b'\rangle\} \\
\mu_{z,1} &= eE_z\{2\langle b|z|b\rangle + \langle a|z|a\rangle\} \\
\mu_{z,2} &= eE_z\{\langle b|z|b\rangle + 2\langle a|z|a\rangle\} \\
\mu_{z,3} &= eE_z\{2\langle b|z|b\rangle + \langle b'|z|b'\rangle\} \\
\mu'_z &= eE_z\langle b|z|b'\rangle
\end{aligned}
$$

Furthermore, the matrix elements are as shown below.

$$
H_{\text{dipole}} = \qquad \text{(A.11)}
$$

$$
\begin{array}{c}
 \\
\mathcal{A}^{0,d}_{+1/2} \\
\mathcal{A}^{0,d}_{-1/2} \\
\mathcal{B}^{1,d}_{+1/2} \\
\mathcal{B}^{1,d}_{-1/2} \\
\mathcal{B}^{2,d}_{+1/2} \\
\mathcal{B}^{2,d}_{-1/2} \\
\mathcal{A}^{3,q}_{+1/2} \\
\mathcal{A}^{3,q}_{-1/2} \\
\mathcal{A}^{3,q}_{+3/2} \\
\mathcal{A}^{3,q}_{-3/2} \\
\mathcal{A}^{3,d'}_{+1/2} \\
\mathcal{A}^{3,d'}_{-1/2} \\
\mathcal{A}^{3,d''}_{+1/2} \\
\mathcal{A}^{3,d''}_{-1/2}
\end{array}
\begin{array}{c}
\begin{array}{cccccccccccccc}
\mathcal{A}^{0,d}_{+1/2} & \mathcal{A}^{0,d}_{-1/2} & \mathcal{B}^{1,d}_{+1/2} & \mathcal{B}^{1,d}_{-1/2} & \mathcal{B}^{2,d}_{+1/2} & \mathcal{B}^{2,d}_{-1/2} & \mathcal{A}^{3,q}_{+1/2} & \mathcal{A}^{3,q}_{-1/2} & \mathcal{A}^{3,q}_{+3/2} & \mathcal{A}^{3,q}_{-3/2} & \mathcal{A}^{3,d'}_{+1/2} & \mathcal{A}^{3,d'}_{-1/2} & \mathcal{A}^{3,d''}_{+1/2} & \mathcal{A}^{3,d''}_{-1/2}
\end{array} \\
\begin{pmatrix}
\mu_{z,1} & & & & & & & & & & & & & \\
0 & \mu_{z,1} & & & & & & & & & & & & \\
-\mu_x & 0 & \mu_{z,2} & & & & & & & & & & & \\
0 & \mu_x & 0 & \mu_{z,2} & & & & & & & & & & \\
\mu'^{*}_x & 0 & 0 & 0 & \mu_{z,3} & & & & & & & & & \\
0 & \mu'^{*}_x & 0 & 0 & 0 & \mu_{z,3} & & & & & & & & \\
0 & 0 & 0 & 0 & 0 & 0 & \mu_{z,0} & & & & & & & \\
0 & 0 & 0 & 0 & 0 & 0 & 0 & \mu_{z,0} & & & & & & \\
0 & 0 & 0 & 0 & 0 & 0 & 0 & 0 & \mu_{z,0} & & & & & \\
0 & 0 & 0 & 0 & 0 & 0 & 0 & 0 & 0 & \mu_{z,0} & & & & \\
\frac{3\mu'^{*}_z}{\sqrt{6}} & 0 & -\frac{3\mu'^{*}_x}{\sqrt{6}} & 0 & 0 & 0 & 0 & 0 & 0 & 0 & 0 & & & \\
0 & \frac{3\mu'^{*}_z}{\sqrt{6}} & 0 & -\frac{3\mu'^{*}_x}{\sqrt{6}} & 0 & 0 & 0 & 0 & 0 & 0 & 0 & 0 & & \\
-\frac{\mu'^{*}_z}{\sqrt{2}} & 0 & -\frac{\mu'^{*}_x}{\sqrt{2}} & 0 & \frac{2\mu'_x}{\sqrt{2}} & 0 & 0 & 0 & 0 & 0 & 0 & 0 & 0 & \\
0 & -\frac{\mu'^{*}_z}{\sqrt{2}} & 0 & -\frac{\mu'^{*}_x}{\sqrt{2}} & 0 & \frac{2\mu'_x}{\sqrt{2}} & 0 & 0 & 0 & 0 & 0 & 0 & 0 & 0
\end{pmatrix}
\end{array}
$$

Appendix B

Magnetic interaction

We define the following values for single molecular orbitals.

$$\begin{aligned} \eta &= \langle a | l_y | b \rangle \\ \eta' &= \langle a | l_y | b' \rangle \end{aligned} \tag{B.1}$$

$$H_{\mathrm{B}} = \frac{\gamma_{\mathrm{e}}\hbar}{2} \times \tag{B.2}$$

	$\mathcal{A}^{0,d}_{+1/2}$	$\mathcal{A}^{0,d}_{-1/2}$	$\mathcal{B}^{1,d}_{+1/2}$	$\mathcal{B}^{1,d}_{-1/2}$	$\mathcal{B}^{2,d}_{+1/2}$	$\mathcal{B}^{2,d}_{-1/2}$	$\mathcal{A}^{3,q}_{+1/2}$	$\mathcal{A}^{3,q}_{-1/2}$	$\mathcal{A}^{3,q}_{+3/2}$	$\mathcal{A}^{3,q}_{-3/2}$
$\mathcal{A}^{0,d}_{+1/2}$	B_z									
$\mathcal{A}^{0,d}_{-1/2}$	$(B_x + iB_y)$	$-B_z$								
$\mathcal{B}^{1,d}_{+1/2}$	$\frac{2B_y}{g_{\mathrm{e}}}\eta$	0	B_z							
$\mathcal{B}^{1,d}_{-1/2}$	0	$\frac{2B_y}{g_{\mathrm{e}}}\eta$	$(B_x + iB_y)$	$-B_z$						
$\mathcal{B}^{2,d}_{+1/2}$	$\frac{2B_y}{g_{\mathrm{e}}}\eta'^{*}$	0	0	0	B_z					
$\mathcal{B}^{2,d}_{-1/2}$	0	$\frac{2B_y}{g_{\mathrm{e}}}\eta'^{*}$	0	0	$(B_x + iB_y)$	$-B_z$				
$\mathcal{A}^{3,q}_{+1/2}$	0	0	0	0	0	0	B_z			
$\mathcal{A}^{3,q}_{-1/2}$	0	0	0	0	0	0	$2(B_x + iB_y)$	$-B_z$		
$\mathcal{A}^{3,q}_{+3/2}$	0	0	0	0	0	0	$\sqrt{3}(B_x - iB_y)$	0	$3B_z$	
$\mathcal{A}^{3,q}_{-3/2}$	0	0	0	0	0	0	0	$\sqrt{3}(B_x + iB_y)$	0	$-3B_z$

Appendix C

Hyperfine interaction

We can write the hyperfine interaction in the form of spherical components as below.

$$\begin{aligned}\hat{V}_{\mathrm{mhf}} &= -C_{\mathrm{mhf}} \sum_i [\hat{J}_i^{(2)} \otimes \hat{A}_i^{(2)}]^{(0)} \\ &= -\frac{C_{\mathrm{mhf}}}{\sqrt{5}} \sum_i \sum_{q=-2}^{q=+2} (-1)^{2-q} J_{i,-q}^{(2)} A_{i,+q}^{(2)}\end{aligned} \tag{C.1}$$

After doing the calculations, we end up with the following Hamiltonian for the ground state (cf. Table C.1).

$$V_{\mathrm{mhf}} = -\frac{C_{\mathrm{mhf}}}{12\sqrt{5}} \begin{array}{c} \\ \Psi_1 \\ \Psi_2 \\ \Psi_3 \\ \Psi_4 \end{array} \begin{array}{c} \begin{array}{cccc} \Psi_1 & \Psi_2 & \Psi_3 & \Psi_4 \end{array} \\ \begin{pmatrix} G_0 & & & \\ 0 & -2G_0 & & \\ -3\sqrt{2}G_1 & 0 & G_0 & \\ 0 & -G_0 & 0 & 0 \end{pmatrix} \end{array} , \tag{C.2}$$

where

$$\begin{aligned} G_0 &= \langle a|(2A_{zz}^{(2)} - A_{xx}^{(2)} - A_{yy}^{(2)})|a\rangle, \\ G_1 &= \langle a|(A_{xx}^{(2)} - A_{yy}^{(2)})|a\rangle. \end{aligned} \tag{C.3}$$

Hyperfine interaction		
Eigenvalues	Eigenstates	Eigenstates in primary basis
$-(1+\sqrt{2})G_0$	$(1+\sqrt{2})\Psi_2+\Psi_4$	$(1+\sqrt{2})\lvert b\bar{b}a-\rangle+\lvert b\bar{b}\bar{a}+\rangle$
$-(1-\sqrt{2})G_0$	$(1-\sqrt{2})\Psi_2+\Psi_4$	$-\lvert b\bar{b}a-\rangle+(1+\sqrt{2})\lvert b\bar{b}\bar{a}+\rangle$
$G_0-3\sqrt{2}G_1$	$\Psi_1+\Psi_3$	$\lvert b\bar{b}a+\rangle+\lvert b\bar{b}\bar{a}-\rangle$
$G_0+3\sqrt{2}G_1$	$-\Psi_1+\Psi_3$	$-\lvert b\bar{b}a+\rangle+\lvert b\bar{b}\bar{a}-\rangle$

Table C.1: Eigensystem of the hyperfine interaction for the ground state in Eq. (C.2). Eigenvalues should be multiplied by $-\frac{C_{\mathrm{mhf}}}{12\sqrt{5}}$.

Appendix D

Calculations of the multiconfiguration states

Here, we use the single-configuration states to estimate the energies of the corresponding multiconfiguration states. We only look at the spin-up quartet and doublet states, but the spin-down calculations are similar. We start with quartet and doublet superposition states.

$$\begin{aligned} |\Psi_q\rangle &= \frac{1}{\sqrt{3}}|\beta\alpha\alpha + \alpha\beta\alpha + \alpha\alpha\beta\rangle \\ |\Psi_{d'}\rangle &= \frac{1}{\sqrt{6}}|\beta\alpha\alpha + \alpha\beta\alpha - 2\alpha\alpha\beta\rangle \\ |\Psi_{d''}\rangle &= \frac{1}{\sqrt{2}}|-\beta\alpha\alpha + \alpha\beta\alpha\rangle \end{aligned} \tag{D.1}$$

state	energy
$\|\alpha\alpha\beta\rangle$	4.7 eV
$\|\beta\alpha\alpha\rangle$	5.4 eV
$\|\alpha\beta\alpha\rangle$	5.5 eV

Table D.1: Electron-spin configurations corresponding to $|bab'\rangle$ and their energies obtained from DFT. α (β) represents spin up (down).

Since $|\alpha\alpha\alpha\rangle$ is also a quartet state, we have $E_q \equiv E[|\Psi_q\rangle] = E[|\alpha\alpha\alpha\rangle]$. By using the equation

$$\frac{1}{\sqrt{3}}(|\Psi_q\rangle - \sqrt{2}|\Psi_{d'}\rangle) = |\alpha\alpha\beta\rangle, \tag{D.2}$$

we have $E[|\alpha\alpha\beta\rangle] = \frac{1}{3}(E_q + 2E[|\Psi_{d'}\rangle])$. Thus, $E_{d'} \equiv E[|\Psi_{d'}\rangle] = (3E[|\alpha\alpha\beta\rangle] - E_q)/2$. Based on our DFT

calculations in Table D.1, $E[|\alpha\alpha\beta\rangle] = 4.7$ eV and $E_q = 4.1$ eV, which implies that $E_{d'} = (3\times 4.7 - 4.1)/2 = 5$ eV. Next, we define auxiliary state ϕ:

$$\begin{aligned} |\phi\rangle &\equiv \frac{1}{2\sqrt{3}}(\sqrt{3}|\Psi_{d'}\rangle + 3|\Psi_{d''}\rangle) \\ &= \frac{1}{2\sqrt{6}}|-2\beta\alpha\alpha + 4\alpha\beta\alpha - 2\alpha\alpha\beta\rangle \\ &= \frac{1}{\sqrt{6}}|-\beta\alpha\alpha + 2\alpha\beta\alpha - \alpha\alpha\beta\rangle. \end{aligned} \tag{D.3}$$

By using this auxiliary state, we show that

$$\frac{1}{\sqrt{3}}(|\Psi_q\rangle + \sqrt{2}|\phi\rangle) = |\alpha\beta\alpha\rangle. \tag{D.4}$$

Similar to previous calculation, we can show that

$$\begin{aligned} E[|\alpha\beta\alpha\rangle] &= \frac{1}{3}(E_q + 2E_\phi) \\ &= \frac{1}{3}\Bigg\{E_q + \frac{1}{6}(3E_{d'} + 9E_{d''} + 3\sqrt{3}\langle\Psi_{d'}|H|\Psi_{d''}\rangle \\ &\qquad + 3\sqrt{3}\langle\Psi_{d''}|H|\Psi_{d'}\rangle)\Bigg\} \\ &= \frac{1}{6}\left\{2E_q + E_{d'} + 3E_{d''}\right\}. \end{aligned} \tag{D.5}$$

Therefore, we can calculate $E_{d''}$ as below.

$$\begin{aligned} E_{d''} &= \frac{1}{3}\left\{6E[|\alpha\beta\alpha\rangle] - 2E_q - E_{d'}\right\} \\ &= \frac{1}{3}(6\times 5.5 - 2\times 4.1 - 5) = 6.6 \text{ eV} \end{aligned} \tag{D.6}$$

Appendix E

ODMR signal

In this chapter, we study the effect of changing parameters used for ODMR signal in Table 5.6 other than those discussed in the main text. In each of the following figures, we change only one or two parameters to see their effect on our model. Figure E.1, shows that for different values of transition rates k_{57} and k_{68} we can see an ODMR signal. In Fig. E.2, we checked the effect of changing the first and the second excited state spin splittings ω_e and ω_{e2}. The result shows that although changing them would affect the magnitude of the ODMR signal, there is only one resonance in the ODMR signal, which suggests that the signals are not narrow enough to distinguish the peaks of ω_e and ω_{e2}. Lastly, Fig. E.3 shows that the spin relaxation times in the range of 0.06 MHz do not have a significant impact on the ODMR signal. Only very large spin relaxation times, which are very unlikely, decrease the ODMR signal.

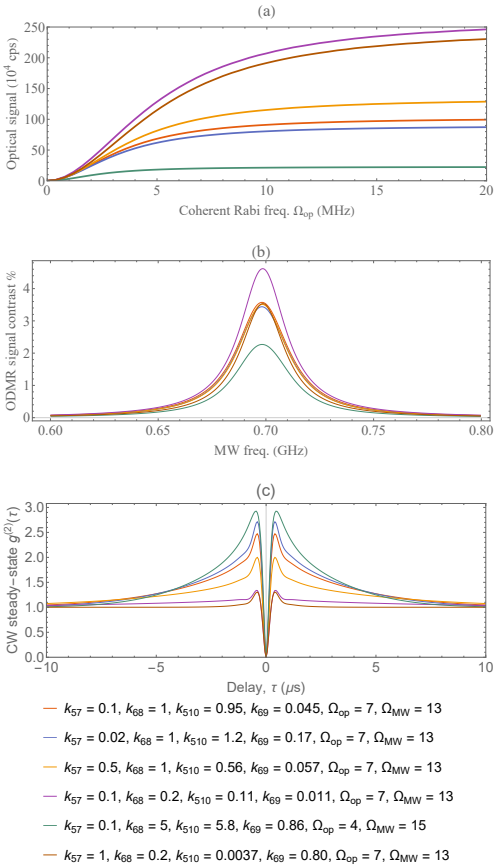

Figure E.1: The effect of changing k_{57} and k_{68} on the optical signal, ODMR contrast, and the second-order correlation function. All the variables are in MHz. Based on the matrix elements of the spin-orbit and spin-spin interactions, the k_{57} and k_{68} rates are related to the k_{510} and k_{69} rates. So changing each of them will affect the other two.

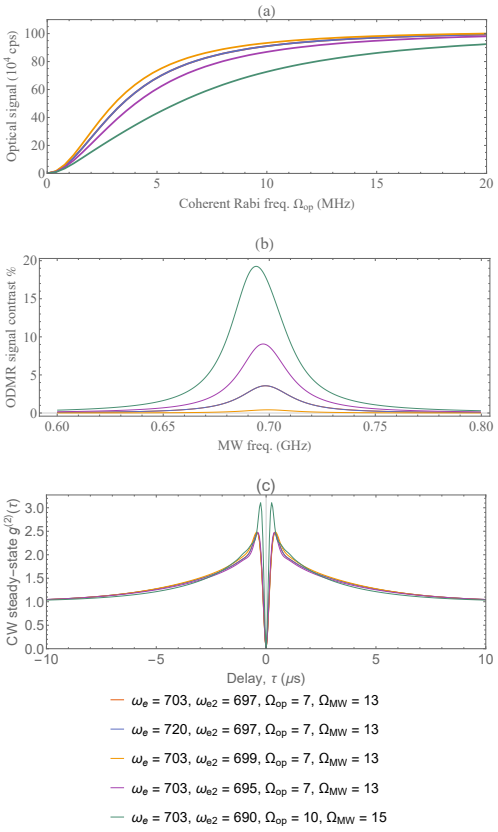

Figure E.2: The effect of changing ω_e and ω_{e2} on the optical signal, ODMR contrast, and the second-order correlation function. All the variables are in MHz.

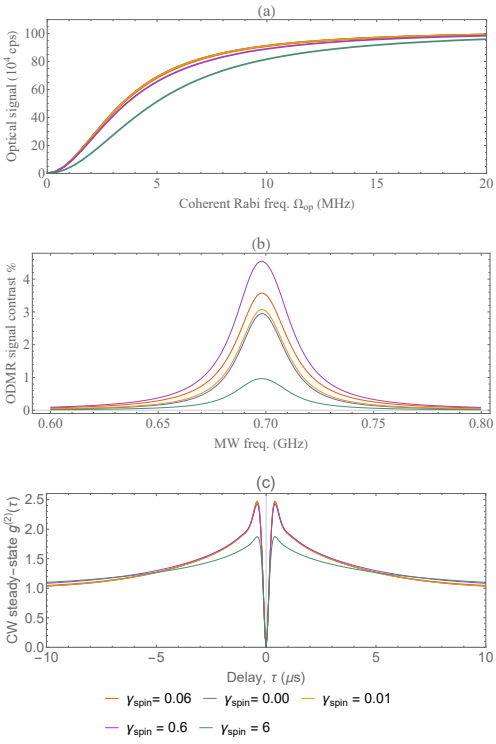

Figure E.3: The effect of changing γ_{spin} on the optical signal, ODMR contrast, and the second-order correlation function. All the variables are in MHz.

Appendix F

Copyright permissions

In this thesis, I have used a paper where I am the first author [1]. Below, I have provided permission from all co-authors via email to include this paper in my thesis (Figs. F.1, F.2, F.3, F.4, F.5, F.6, and F.7). Also, Physical Review B grants the permission to authors to use the materials in their paper as long as proper citation is provided (Fig. F.8).

From: Christoph Simon
Sent: Wednesday, June 15, 2022 8:16 AM
To: Omid Aligholamioskooee
Subject: Re: Permission to reuse our h-BN paper

Yes, of course!
Christoph

From: Omid Aligholamioskooee
Sent: June 15, 2022 8:09 AM
To: Christoph Simon
Subject: Permission to reuse our h-BN paper

Hi Christoph,

Sorry, I had forgotten to ask your permission to reuse our h-BN paper in my thesis. I need to attach an email of confirmation from all the coauthors. Is that fine with you?

Cheers,
Omid

Figure F.1: Permission from Christoph Simon.

From: Ken Sharman
Sent: Friday, April 22, 2022 4:36 PM
To: Omid Aligholamioskooee
Subject: Re: Permission for using our h-BN paper in my thesis

Of course! Let me know if you need anything to make it happen.

Ken

From: Omid Aligholamioskooee
Sent: April 22, 2022 4:27 PM
To: Ken Sharman
Subject: Permission for using our h-BN paper in my thesis

Dear Ken,

I want to use our h-BN paper as part of my master's thesis. I would like to know if it's ok with you and if you give me permission to use it or not?

Best,
Omid

Figure F.2: Permission from Kenneth Sharman.

From: Roohollah Ghobadi
Sent: Friday, April 22, 2022 9:37 PM
To: Omid Aligholamioskooee
Subject: Re: Permission for using our h-BN paper in my thesis

Dear Omid, of course, permission granted 🙂

Cheers,
Farid

From: Omid Aligholamioskooee
Sent: Friday, April 22, 2022 4:27 PM
To: Roohollah Ghobadi
Subject: Permission for using our h-BN paper in my thesis

Dear Farid,

I want to use our h-BN paper as part of my master's thesis. I would like to know if it's ok with you and if you give me permission to use it or not?

Best,
Omid

Figure F.3: Permission from Roohollah Ghobadi.

From: Stephen Wein
Sent: Saturday, April 23, 2022 1:31 AM
To: Omid Aligholamioskooee
Subject: Re: Permission for using our h-BN paper in my thesis

[△EXTERNAL]

Hi Omid,

Of course! You have my full permission to use it.

Cheers,
Stephen

On Sat., Apr. 23, 2022, 12:28 a.m. Omid Aligholamioskooee wrote:

> Dear Stephen,
>
> I want to use our h-BN paper as part of my master's thesis. I would like to know if it's ok with you and if you give me permission to use it or not?
>
> Best,
>
> Omid

Figure F.4: Permission from Stephen C. Wein.

From: Hadi Zadeh Haghighi
Sent: Thursday, April 21, 2022 2:03 PM
To: Omid Aligholamioskooee
Subject: Re: Permission for using our paper in my thesis

Dear Omid,

Absolutely, you have my permission to include it in your thesis.

For including a paper in your thesis, besides permissions from the co-authors, you need to provide a piece of proof that the journal also allows you to do so (this should be on their website, and a screenshot suffices).

Cheers,
Hadi

From: Omid Aligholamioskooee
Sent: Thursday, April 21, 2022 10:30
To: Hadi Zadeh Haghighi
Subject: Permission for using our paper in my thesis

Dear Hadi,

I want to use our paper as part of my master's thesis. First, I would like to know if it's ok with you and you give the permission to use it or not? Also, Christoph told me to talk to you about the asking for permission process; I think he meant for the journal, but anything that might help me. Could you please walk me through it?

Cheers,
Omid

Figure F.5: Permission from Hadi Zadeh-Haghighi.

From: Claudia Gomes da Rocha
Sent: Friday, April 22, 2022 4:07 PM
To: Omid Aligholamioskooee
Subject: Re: Permission for using our h-BN paper in my thesis

Hello Omid,

of course you can use it.

Claudia

From: Omid Aligholamioskooee
Sent: Friday, April 22, 2022 3:38 PM
To: Claudia Gomes da Rocha
Subject: Permission for using our h-BN paper in my thesis

Dear Claudia,

I want to use our h-BN paper as part of my master's thesis. I would like to know if it's ok with you and if you give me permission to use it or not?

Best,
Omid

Figure F.6: Permission from Claudia Gomes da Rocha.

From: Dennis Salahub
Sent: Friday, April 22, 2022 3:55 PM
To: Omid Aligholamioskooee
Subject: Re: Permission for using our h-BN paper in my thesis

Permission granted!

Best

Dennis

From: Omid Aligholamioskooee
Sent: Friday, April 22, 2022 3:36:56 PM
To: Dennis Salahub
Subject: Permission for using our h-BN paper in my thesis

Dear Dennis,

I want to use our h-BN paper as part of my master's thesis. I would like to know if it's ok with you and if you give me permission to use it or not?

Best,
Omid

Figure F.7: Permission from Dennis R. Salahub.

From: APS Help Desk
Sent: Wednesday, April 27, 2022 7:56 AM
To: Omid Aligholamioskooee
Subject: [APS] Re: Fwd: BK14220 - Permission to reprint

[△EXTERNAL]

Jessica Stepnoski (APS)

Apr 27, 2022, 9:56 AM EDT

Dear Dr. Aligholamioskoo,

Authors of published manuscripts do not need permission from APS to reuse any of their published content. However, the appropriate bibliographic citation must be included as follows.

The following are the terms and conditions that come with APS's copyright permissions:

"For electronic format permissions, Requestor agrees to provide a hyperlink from the reprinted APS material using the source material?s DOI on the web page where the work appears. The hyperlink should use the standard DOI resolution URL, http://dx.doi.org/{DOI} (http://dx.doi.org/%7BDOI%7D) . The hyperlink may be embedded in the copyright credit line.

"For print format permissions, Requestor agrees to print the required copyright credit line on the first page where the material appears: "Reprinted (abstract/excerpt/figure) with permission from [(FULL REFERENCE CITATION) as follows: Author's Names, APS Journal Title, Volume Number, Page Number and Year of Publication.] Copyright (YEAR) by the American Physical Society.""

I hope this is helpful to you.
Please let us know if you should need any further assistance.

Figure F.8: Permission from Physical Review B.